Draft version November 5, 2015
Preprint typeset using LaTeX style emulateapj v. 03/07/07

EDDINGTON RATIO DISTRIBUTION OF X-RAY SELECTED BROAD-LINE AGNS AT $1.0 < Z < 2.2$[†]

Hyewon Suh[1], Günther Hasinger[1], Charles Steinhardt[2,3], John D. Silverman[3], and Malte Schramm[4,3]
[1] Institute for Astronomy, University of Hawaii, 2680 Woodlawn Drive, Honolulu, HI 96822, USA
[2] California Institute of Technology, 1200 East California Boulevard, Pasadena, CA 91125, USA
[3]Kavli Institute for the Physics and Mathematics of the Universe, Todai Institutes for Advanced Study, the University of Tokyo, Kashiwa, Japan 277-8583 (Kavli IPMU, WPI)
[4]National Astronomical Observatory of Japan, Mitaka, Tokyo 181-8588, Japan
Draft version November 5, 2015

ABSTRACT

We investigate the Eddington ratio distribution of X-ray selected broad-line active galactic nuclei (AGN) in the redshift range $1.0 < z < 2.2$, where the number density of AGNs peaks. Combining the optical and Subaru/FMOS near-infrared spectroscopy, we estimate black hole masses for broad-line AGNs in the *Chandra* Deep Field-South (CDF-S), Extended *Chandra* Deep Field-South (E-CDF-S), and the *XMM-Newton* Lockman Hole (*XMM*-LH) surveys. AGNs with similar black hole masses show a broad range of AGN bolometric luminosities, which are calculated from X-ray luminosities, indicating that the accretion rate of black holes is widely distributed. We find that a substantial fraction of massive black holes accreting significantly below the Eddington limit at $z \lesssim 2$, in contrast to what is generally found for luminous AGNs at high redshift. Our analysis of observational selection biases indicates that the "AGN cosmic downsizing" phenomenon can be simply explained by the strong evolution of the co-moving number density at the bright end of the AGN luminosity function, together with the corresponding selection effects. However, it might need to consider a correlation between the AGN luminosity and the accretion rate of black holes that luminous AGNs have higher Eddington ratios than low-luminosity AGNs in order to understand the relatively small fraction of low-luminosity AGNs with high accretion rates in this epoch. Therefore, the observed downsizing trend could be interpreted as massive black holes with low accretion rates, which are relatively fainter than less massive black holes with efficient accretion.
Subject headings: galaxies: active — galaxies: nuclei — quasars: general — black hole physics

1. INTRODUCTION

Disentangling the origin and the mass accretion history of black holes is one of the most outstanding issues for understanding the fundamental processes of galaxy formation and evolution. Observations have shown that supermassive black holes are tightly linked with their host galaxies, as revealed by correlations between the black hole mass and the bulge stellar mass, i.e., $M_{BH} - M_{stellar}$ relation (Kormendy & Richstone 1995; Magorrian et al. 1998; Gültekin et al. 2009; Schulze & Gebhardt 2011; McConnell & Ma 2013) and the velocity dispersion, i.e., $M_{BH} - \sigma$ relation (Ferrarese & Merritt 2000; Gebhardt et al. 2000; Merritt & Ferrarese 2001; Tremaine et al. 2002; Gültekin et al. 2009; Graham et al. 2011; McConnell & Ma 2013; Woo et al. 2013). Furthermore, it has been widely accepted that the growth of active galactic nuclei (AGN) and the star formation history undergo very similar evolutionary behavior through cosmic time, where the peaks of most luminous AGNs and powerful star-forming galaxies occur at a similar cosmic epoch ($z = 2 - 3$) with a dramatic decline towards low redshift, while the moderate-luminosity AGNs and the bulk of star-forming galaxies peak at lower redshift ($z \lesssim 1$) (see e.g. Shankar et al. 2009; Madau & Dickinson 2014). This seems to imply that the interaction between the nuclear activity and the star formation in galaxies plays a crucial role in the evolution of black holes and galaxies over cosmic time.

The AGN luminosity function and its evolution are key observational properties for understanding the accretion history onto the black holes. Observational studies have revealed a "cosmic downsizing" or "anti-hierarchical" phenomenon in the black hole growth, which means that the characteristic luminosity of AGNs decreases with time. The co-moving number density of luminous AGNs peaks at higher redshift ($z \sim 2$) than moderate-luminosity AGNs, which peaks at $z < 1$ (Giacconi et al. 2002; Cowie et al. 2003; Steffen et al. 2003; Ueda et al. 2003; Barger et al. 2005; Hasinger et al. 2005; La Franca et al. 2005; Hopkins et al. 2007; Silverman et al. 2008a). This AGN cosmic downsizing trend is seen across a wide range of the electromagnetic spectrum in X-ray, optical, infrared, and radio wavebands (Bongiorno et al. 2007; Cirasuolo et al. 2007). If AGN luminosity would strictly correlate with black hole mass, this finding would imply that more massive black holes formed before lower-mass black holes, which is in apparent contradiction to the currently favored hierarchical structure formation paradigm based on the standard cold dark matter model. In the hierarchical framework, more massive halos grow over time hierarchically via subsequent merging and smooth accretion among low mass halos.

The AGN cosmic downsizing, however, is observed in luminosity, and thus the downsizing phenomenon can also be interpreted assuming a relationship between the AGN luminosity and the black hole mass as a function of redshift. Black holes are assumed to undergo several

[†] Based in part on data collected at Subaru Telescope, which is operated by the National Astronomical Observatory of Japan.

episodes of a significant gas accretion with complex hydrodynamic and magnetic processes, along with relativistic effects during which this accretion powers AGNs (e.g. Springel et al. 2005; Choi et al. 2012). The most luminous AGNs are interpreted as results of major mergers. A substantial starburst occurs as a result of major mergers, and some of the gas eventually reaches the black hole at the center of a galaxy, triggering the AGN activity (see e.g. Di Matteo et al. 2005). On the other hand, moderate-luminosity AGNs are suggested to be products of modest accretion, in which case the gas accretion via internal, secular processes trigger the AGN activity (e.g. Hopkins & Hernquist 2006; Fanidakis et al. 2012). An AGN with black hole mass of M_{BH} can produce the maximum luminosity via the Eddington limit (L_{Edd}) at which the radiation pressure by the accretion of the infalling matter balances the gravitational attraction of the black hole for spherically symmetric time-invariant accretion. By estimating the Eddington ratios, the ratio of the AGN bolometric luminosity and the Eddington luminosity (L_{bol}/L_{Edd}), it can be determined whether the accretion rate of black holes can change over cosmic time. One might have expected a correlation between black hole masses and AGN bolometric luminosities, but if there is a range in accretion rates and/or efficiencies, the relation will be weaker. Thus, in order to investigate the observed downsizing trend in black hole growth, it is important to explore the efficiency of gas accretion during the active phases of black holes. Therefore, the black hole mass and the bolometric luminosity are the key parameters to understanding the evolutionary picture for AGNs.

Large, modern photometric and spectroscopic surveys open up a new regime for studying a large sample of AGNs (e.g. Sloan Digital Sky Survey (SDSS), Schneider et al. 2010; Shen et al. 2011). Many efforts have been made to describe the properties of thousands of AGNs (e.g. McLure & Dunlop 2004; Vestergaard & Osmer 2009; Steinhardt & Elvis 2010; Choi et al. 2014). In previous studies, the Eddington ratio has been assumed to be close to the Eddington limit regardless of redshift and luminosities. Marconi et al. (2004) suggest that the Eddington ratios of local black holes are in the range between 0.1 and 1.7, suggesting that black hole growth takes place during luminous accretion phases close to the Eddington limit at high redshift. Kollmeier et al. (2006) present that the AGN population is dominated by narrowly distributed near-Eddington accretion rate objects, with a median of 0.1 and a dispersion of 0.3 dex, also suggesting that supermassive black holes gain most of their mass while radiating close to the Eddington limit. However, it is difficult to draw any conclusions about the underlying distribution of the Eddington ratio because the shallowness of the large wide area surveys imposes severe restrictions on the combinations of AGN luminosities and black hole masses that are observable, especially at $z > 1$. Recent studies have shown that there is a wide spread in the range of the Eddington ratios (e.g. Babić et al. 2007; Fabian et al. 2008; Schulze & Wisotzki 2010; Kelly et al. 2010). Lusso et al. (2012) find that the Eddington ratio increases with redshift for AGNs at any given black hole masses. They also show that the Eddington ratio increases with AGN bolometric luminosity, while no clear evolution with redshift is seen. A wide range of Eddington ratios indicates that their luminosity is not directly related to the black hole mass. Therefore, it is necessary to consider a wide range of Eddington ratios with respect to the AGN luminosity and the black hole mass in order to understand the accretion growth history of the black holes.

Unfortunately, the detailed follow-up study in the redshift interval $z = 1 - 2$, where the AGN downsizing appears, has been difficult because of the lack of emission line diagnostics in the optical wavelength range, which is often referred to as the redshift desert. The strong Balmer emission lines, Hα and Hβ, are redshifted to 13126Å and 9722Å at z=1, respectively. The advent of the sensitive near-infrared (NIR) spectrograph Fiber Multi Object Spectrograph (FMOS) on the Subaru telescope finally enables us to determine the black hole mass in the key redshift interval $z = 1 - 2$ using the Balmer lines that are the same lines for which the black hole masses are calibrated at low redshift. This redshift range is of particular interest, as it is the epoch that a significant part of the accretion growth of black holes takes place, where the AGN density peaks and where optical spectroscopy cannot easily determine the redshifts and properties of many of the AGNs.

In this paper, we investigate the Eddington ratios for X-ray selected broad-line AGNs in the *Chandra* Deep Field-South (CDF-S), Extended *Chandra* Deep Field-South (E-CDF-S), and the *XMM*-Newton Lockman Hole (*XMM*-LH) fields. Absorption-corrected X-ray luminosities together with bolometric corrections will allow an estimate of bolometric luminosities of AGNs. The advantage of using X-ray luminosities to derive AGN bolometric luminosities is that they are relatively less affected by the presence of obscuration and contamination effects from the host galaxy. We determine black hole masses using Subaru/FMOS NIR spectroscopic observations and available optical spectroscopy from the literature. We also investigate the possible biases due to systematics and selection effects on the observed data.

Throughout this paper we assume a ΛCDM cosmology with $\Omega_m = 0.3$, $\Omega_\Lambda = 0.7$ and $H_0 = 70$ km s^{-1} Mpc^{-1}.

2. SAMPLE SELECTION

An X-ray survey is practically the most efficient way of finding AGNs over a wide range of luminosities and redshifts. The deep surveys with *Chandra* (i.e., *Chandra* Deep Field-North and *Chandra* Deep Field-South; see Brandt & Hasinger 2005; Brandt & Alexander 2010) and *XMM-Newton* (i.e., Lockman Hole; see Hasinger et al. 2001; Rovilos et al. 2011) allow us to detect a fair sample of low-luminosity ($42 < \log L_X < 44$) AGNs out to $z \sim 5$, providing a unique opportunity of studying AGN evolution. Besides, these fields are the best window for the deepest and cleanest images at a variety of wavelengths due to the remarkably low Galactic line-of-sight HI column density (i.e., $N_H = 8.8 \times 10^{19}$ cm^{-2} for CDF-S; Stark et al. 1992, $N_H = 5.7 \times 10^{19}$ cm^{-2} for *XMM*-LH; Lockman et al. 1986).

We start by selecting a sample of AGNs based on comprehensive catalogs of X-ray sources observed in the CDF-S, E-CDF-S, and *XMM*-LH fields, described below.

2.1. *Chandra Deep Field South*

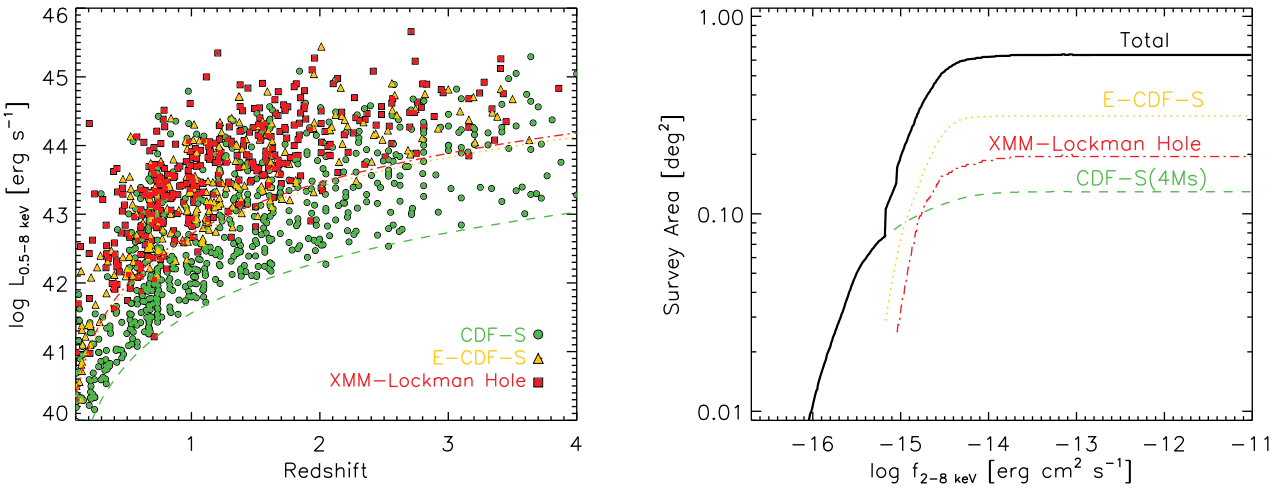

FIG. 1.— *Left:* The absorption-corrected 0.5-8 keV X-ray luminosity versus redshift (spectroscopic or photometric) from the X-ray surveys as labeled. *Right:* Survey area coverage as a function of X-ray flux. The black line represent the total combined area of all surveys.

The catalog for the 4 Ms CDF-S, which is the deepest *Chandra* survey covering an area of 464.5 arcmin^2, contains 740 X-ray sources providing the most sensitive $0.5-8$ keV view of the distant universe (Xue et al. 2011). The survey reaches flux limits of 3.2×10^{-17}, 9.1×10^{-18}, and 5.5×10^{-17} erg cm^{-2} s^{-1} for the full ($0.5-8$ keV), soft ($0.5-2$ keV), and hard ($2-8$ keV) bands, respectively. 674 out of the 740 main-catalog sources have either spectroscopic or photometric redshifts, yielding an overall redshift completeness of ∼91%.

In addition to the 4Ms CDF-S point source catalog, we make use of the E-CDF-S observations that have been analyzed and cataloged by Lehmer et al. (2005) and Silverman et al. (2010), providing a sample of 762 distinct X-ray point sources with either spectroscopic or photometric redshifts. Of the 762 E-CDF-S main catalog sources, 523 sources were used since 239 sources were also present in the 4 Ms CDF-S catalog. We have an excellent redshift completeness of ∼95% (498/523). This survey reaches sensitivity limits of 1.1×10^{-16} and 6.7×10^{-16} ergs cm^{-2} s^{-1} for the soft ($0.5-2.0$ keV) and hard ($2-8$ keV) bands, respectively.

2.2. *XMM-Newton Lockman Hole*

The catalog of the 409 *XMM*-LH X-ray sources is presented in Brunner et al. (2008), with sensitivity limits of 1.9×10^{-16}, 9×10^{-16}, and 1.8×10^{-15} erg cm^{-2} s^{-1} in the soft ($0.5-2$ keV), hard ($2-10$ keV), and very hard ($5-10$ keV) bands, respectively. Fotopoulou et al. (2012) provide spectroscopic or photometric redshifts for the *XMM*-LH X-ray sources. There is a reasonably high redshift completeness with 92% (376 out of 409). Although the sensitivity limit of the *XMM*-LH survey is much higher than that of the *Chandra* survey, the larger field of view of *XMM*-LH (25×25 arcmin^2) offers a significant sample of bright AGNs while the CDF-S observation provides the fainter tail of AGNs.

2.3. *X-ray selected AGN Sample*

We generate a total of 1548 X-ray selected AGNs which have reliable spectroscopic or photometric redshift identifications from the X-ray catalogs containing a total of 1672 X-ray sources. We show the X-ray sources with either spectroscopic or photometric redshift from the X-ray surveys as labeled in Figure 1. The absorption-corrected $0.5-8$ keV X-ray luminosity of AGNs as a function of redshift (spectroscopic or photometric) is shown in the left panel of Figure 1. The luminosity of AGNs in the redshift range $1.0<z<2.2$ is distributed between $L_{0.5-8\ keV}=10^{42.5}$ and $10^{45.5}$erg/s. In the right panel, we show the sky coverage for the individual surveys and the total sample used. As shown, the total sky area is ~0.7 deg^2 with the narrow deep CDF-S field and the shallower wide-area E-CDF-S and XMM-LH surveys. The deep CDF-S survey improves the AGN sample at low luminosities, while the E-CDF-S and XMM-LH surveys, of shallower depth but of wider area, effectively supply the more luminous AGNs.

3. SPECTROSCOPIC DATA

3.1. *Subaru/FMOS Near-Infrared Observations*

We performed NIR spectroscopic observations for the AGN sources with the FMOS (Kimura et al. 2010) high-resolution spectrographs on the Subaru telescope. FMOS provides up to 400 1.2″ diameter fibers in the circular 30′ diameter field of view. In the high resolution mode, the FMOS spectral coverage is divided into four bands, which are J-short ($0.92-1.12$ μm), J-long ($1.11-1.35$ μm), H-short ($1.40-1.60$ μm), and H-long ($1.60-1.80$ μm) with a spectral resolution of R= $\lambda/\Delta\lambda\sim2200$. The Cross-Beam Switching (CBS) mode, in which two fibers are allocated to each target, was used for optimal sky subtraction of faint sources. The fibers in each pair are separated by 60 arcseconds, alternating between one for the target and the other one simultaneously placed on the sky, so that sky subtraction is not affected by time variation of sky brightness.

The primary targets are X-ray selected AGNs in the CDF-S, E-CDF-S, and *XMM*-LH surveys with either spectroscopic or photometric redshifts in the range $1.0<z<2.2$, and J magnitudes brighter than 22.5 mag.

TABLE 1
SUBARU FMOS Spectroscopic Observations

Date	Field	Spectrograph
2012 Mar 25	XMM-LH	J-long
2012 Mar 26	XMM-LH	H-long
2012 Dec 28	CDF-S	J-long
2012 Dec 29	CDF-S, XMM-LH	H-short
2012 Dec 30	CDF-S, XMM-LH	H-long
2013 Jan 19	CDF-S	H-long
2013 Jan 20	CDF-S	J-long
2013 Jan 21	CDF-S	J-long
2013 Feb 24	XMM-LH	H-short
2013 Oct 23	CDF-S	J-long
2013 Oct 24	CDF-S	H-long

The FMOS J-band and H-band observations cover the Hα and/or Hβ lines in the redshift range $z = 0.7 - 2.7$. The data was obtained during 2012-2013, shown in Table 1. We observed for a total integration time of 3.5−4 hours while accumulating 28-30 frames with an exposure time of 900 seconds per frame. The weather conditions were acceptable, with seeing typically in the range of 0.″6 to 1.″2.

We reduced the data using the publicly available software FIBRE-pac (FMOS Image-Based REduction package; Iwamuro et al. 2012), which is an IRAF-based reduction tool for FMOS. This procedure includes background subtraction, corrections of detector cross talk, bias difference, bad pixels, the spectral distortion, and the removal of residual airglow lines. Individual frames were combined into an ensemble image, and wavelength and flux calibration were carried out. For the absolute flux calibration, the bright (J_{AB}=15-18 mag) stars in each frame were used as a spectral reference. The flux of the reference star was estimated and compared with the photometric data in the catalog. All the spectra were divided by the reference spectrum, and then multiplied by the expected spectrum of the reference star. Apart from the calibration of slit losses through the spectroscopic reference star we do not apply further calibration corrections for our sample of AGNs, since we assume that the reference star corrects most of the slit losses for the point-like sources. While systematic effects like weather conditions, position accuracy still may cause differential flux losses across the field of view, the effect of these systematic errors on black hole masses should be small, since the black hole mass is a function of the square root of the luminosity (see Section 5.2). Finally, the one-dimensional spectrum of each object was extracted from the calibrated image, together with the associated noise spectra.

With the fully reduced 1- and 2-dimensional spectra, we determined the redshift through the identification of prominent emission line features. Each spectrum was visually inspected by Suh and Hasinger individually using the SpecPro (Masters & Capak 2011) environment, which is an IDL-based interactive program for viewing and analyzing spectra. We assigned a quality flag to each redshift to indicate the reliability of the redshift determination. Altogether 825 X-ray sources were observed in the combined CDF-S, E-CDF-S, and *XMM*-LH fields, of which 262 sources are spectroscopically identified. It is noteworthy that we identified new spectroscopic redshifts for 135 X-ray selected AGNs. The redshift identifications are summarized in Appendix Table 2.

3.2. *Optical spectroscopy*

In addition to NIR spectra, we use existing optical spectroscopy that includes a detection of a broad Mg II emission line, shown to be a reliable probe of black hole mass at $z > 1$ (e.g. McLure & Jarvis 2002; Shen & Liu 2012; Matsuoka et al. 2013). Optical spectroscopy has been obtained in the CDF-S, E-CDF-S, and *XMM*-LH fields (Lehmann et al. 2000, 2001; Szokoly et al. 2004; Silverman et al. 2010; Barger et al. 2014, priv. comm.), providing spectroscopic redshifts for X-ray sources. Szokoly et al. (2004) present the results of spectroscopic follow-up for the CDF-S, which were observed at the VLT with the FORS1/FORS2 spectrographs for *Chandra* sources. Furthermore, Silverman et al. (2010) provide high-quality optical spectra in the E-CDF-S. 283 *Chandra* sources are observed with deep exposures (2-9 hr per pointing) using multi-slit facilities on both VLT/VIMOS and Keck/DEIMOS. Lehmann et al. (2000, 2001) offer spectroscopy of the ROSAT Deep Surveys in the Lockman Hole using low-resolution Keck spectra. We compile the existing optical observations of X-ray AGNs from these deep spectroscopic surveys.

4. AGN BOLOMETRIC LUMINOSITY

The bolometric luminosity of AGNs can be estimated from the X-ray luminosity by applying a suitable bolometric correction. In order to estimate an accurate total intrinsic luminosity radiated by the AGN accretion disc, it is necessary to constrain the absorption-corrected intrinsic X-ray luminosity because it is often obscured and also includes reprocessed radiation. We thus derive the absorption corrected rest-frame X-ray luminosity and determine the bolometric luminosity with the bolometric correction. To account for the dependence of the optical to X-ray flux ratio α_{ox} on luminosity, we use the luminosity-dependent bolometric correction factor (see e.g. Vignali et al. 2003; Marconi et al. 2004; Hopkins et al. 2007; Lusso et al. 2012). Despite some difference between the luminosity-dependent bolometric correction factor among different studies (e.g. Lusso et al. 2012 predicted lower bolometric correction at high bolometric luminosity with respect to that predicted by Marconi et al. 2004 and Hopkins et al. 2007), the same trend of increasing bolometric correction at increasing bolometric luminosity is observed within the scatter.

We compute the intrinsic X-ray luminosity of broad-line AGNs following Xue et al. (2011). As a first step, we assume the intrinsic X-ray spectrum of AGNs modeled by a power-law component with both intrinsic and Galactic absorption (i.e., *zpow* × *wabs* × *zwabs* in XSPEC) to estimate the intrinsic column density. A power-law photon index of $\Gamma = 1.8$, which is typical for intrinsic AGN spectra, is assumed and the redshifts of the *zpow* and *zwabs* components are fixed to that of the source. We additionally fixed the Galactic column density to $N_H = 6.0 \times 10^{19}$ cm^{-2}. We then derive the intrinsic column density that reproduces observed hard ($2 - 8$ keV) and soft ($0.5 - 2$ keV) band hardness ratios using XSPEC. The intrinsic X-ray luminosity is derived from the equation $L_X = 4\pi d_L^2 \ f_{X,int} \ (1+z)^{\Gamma-2}$ by correcting both intrinsic and

Galactic absorption. $f_{\rm X,int}$ is the absorption-corrected X-ray flux and the d_L is luminosity distance. Finally, we derive the bolometric luminosity of AGNs from the absorption-corrected rest-frame intrinsic X-ray luminosity with the luminosity-dependent bolometric correction factor described in Marconi et al. (2004). They derived the bolometric corrections from an AGN template spectrum of optical-ultraviolet and X-ray luminosities radiated by the accretion disc and hot corona. They considered only the AGN accretion powered luminosity, neglecting the luminosity reprocessed by the dust, which is therefore representative of the AGN accretion power. The scatter is given by ~ 0.1 for X-ray luminosities.

5. BLACK HOLE MASS ESTIMATION

The black hole mass can be estimated using the broad-line width and the continuum (or line) luminosity from their single-epoch spectra as proxies for the characteristic velocity and the size of the broad-line region (e.g., Kaspi et al. 2000; Vestergaard 2002; Woo & Urry 2002; McLure & Jarvis 2002; McLure & Dunlop 2004; Greene & Ho 2005; Kollmeier et al. 2006; Vestergaard & Peterson 2006; Shen et al. 2008, 2011). Depending on the redshift, single-epoch virial black hole masses have been estimated from different broad emission lines, such as Mg II (McLure & Jarvis 2002; McLure & Dunlop 2004; McGill et al. 2008; Vestergaard & Osmer 2009; Wang et al. 2009; Shen et al. 2011; Rafiee & Hall 2011), Hβ (Greene & Ho 2005; Vestergaard & Peterson 2006), and Hα (Greene & Ho 2005; Matsuoka et al. 2013) lines. The virial black hole masses are calibrated against the black hole mass estimated by the reverberation mapping or that from the single-epoch broad-line width of Hβ emission line in the local universe. Although there are several systematic uncertainties in these single-epoch virial black hole mass estimators, a number of studies have shown that there is consistency in black hole masses from various estimators. Shen & Liu (2012) point out that there is essentially no difference in black hole mass estimates using Mg II and the Balmer lines for high redshift luminous AGNs. Matsuoka et al. (2013) also show that virial black hole masses based on Hα and Mg II emission lines are very similar over a wide range in black hole mass. They suggest that local scaling relations, using Hα or Mg II emission lines, are applicable for moderate-luminosity AGNs up to $z \sim 2$.

We measure the properties of broad emission lines (e.g., Hα, Hβ, and Mg II) present in optical and NIR spectra to derive single-epoch virial black hole mass of broad-line AGNs. The Hα λ6563Å and the Hβ λ4861Å lines are redshifted to the NIR range, and the Mg II λ2798Å line is present in optical spectra in the redshift range $0.5 < z < 2.5$.

5.1. *Spectral line fitting*

We perform a fit to the emission lines using the mpfit routine, which adopts a Levenberg-Marquardt least-squares minimization algorithm to derive the best-fit parameters as well as a measure of the goodness of the overall fit. We specifically measure the width and the luminosity of emission lines in the case of Hα and Hβ lines, and the width and the monochromatic continuum luminosity at 3000Å in the case of the Mg II line. There might be a non-negligible host galaxy contribution at 3000Å continuum luminosity, but we do not correct for any contamination by the host galaxy and extinction due to dust. While we should be aware of this issue, the impact of these on black hole masses should be small, since the black hole mass scales with the square root of the luminosity (see Section 5.2).

Broad-line AGN spectra in the wavelength region of interest are usually characterized by a power-law continuum, $f_\lambda \propto \lambda^{-\alpha}$, and broad (and/or narrow) emission line components. We begin by fitting a power-law continuum with a slope of the continuum as a free parameter. In the case of the Mg II line, it is crucial to consider a complex of Fe II emission lines because in this wavelength range the lines are strongly blended with the broad Fe II emission features (e.g. Vestergaard & Wilkes 2001; Matsuoka et al. 2007; Harris et al. 2013). We simultaneously fit the combination of a power-law continuum and Fe II emission components. An empirical Fe II emission template is adopted from Vestergaard & Wilkes (2001) and convolved with Gaussian profiles of various widths. We left the width, normalization, and offset from the line center as free parameters during the fit. From the best-fit power-law continuum, we derive an estimate of monochromatic luminosity at 3000Å. Finally, we subtract the best-fit power-law continuum (and/or the Fe II emission components) from the spectra.

We further consider individual components to determine the pure broad-line components that enable an accurate determination of the virial black hole masses. The line profile is described by a combination of multiple Gaussian components to best characterize the line shape in the sense that broad emission lines in AGNs can have a complex shape (e.g. Collin et al. 2006). The multiple Gaussian components provide non-Gaussian, asymmetric profiles reproducing the observed broad-line profile smoothly, but we are not concerned with the physical significance of the individual components. We fit the Hα λ6563Å (Hβ λ4861Å) line with one or two broad and a narrow Gaussian components, and the [N II] λ6548,6583Å ([O III] λ4959,5007Å) lines with a pair of Gaussians. The line ratio of the [N II] λ6548,6583Å and the [O III] λ4959,5007Å lines are fixed to the laboratory value of 2.96 and 2.98, respectively. Both the narrow width of the [N II] and the [O III] lines are fixed to match the narrow component of Hα and Hβ, respectively. We left the FWHM of the narrow line components as free parameters but limited to 900 km/s. For the Mg II line, we fit with one or two broad Gaussians components. We do not consider the doublet component of the Mg II line because the line separation is small and does not affect the broad-line width.

As a consistency check we compare the fit of the Mg II line with Fe II emission components to that of the Hα line, since the Hα line is not affected by Fe II emission. In Figure 2, we show an example fit of the Hα line and that of the Mg II line with/without Fe II broad emission component for the same AGN source '*XMM*-LH 270' at $z = 1.576$. We show the observed spectrum (grey) with the best fit (black) of the Hα line (top panel) and the Mg II line (bottom panel). The different components are also indicated as red gaussian curves (broad-line components), blue curves (narrow-line components of

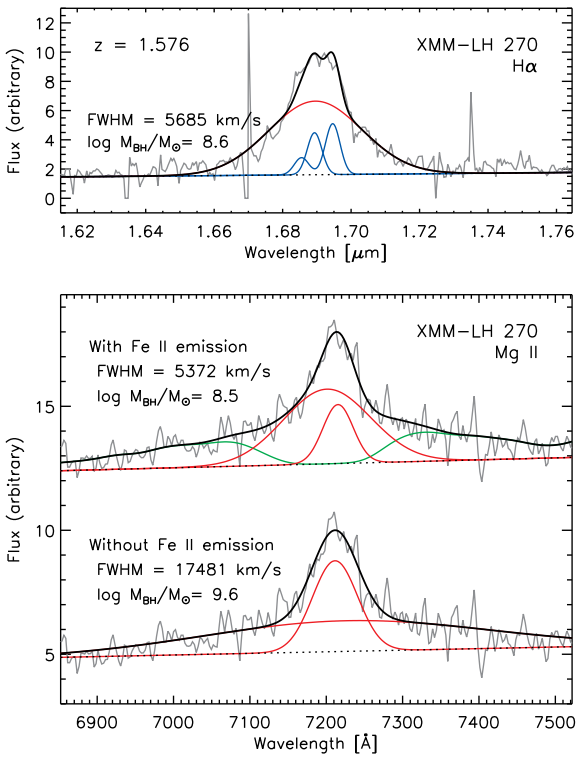

FIG. 2.— Comparison of the broad-line fit for the Hα line (top panel) with that of the Mg II line (bottom panel) with/without a Fe II broad emission component for the same AGN source '*XMM*-LH 270' at $z = 1.576$. The observed spectrum (grey) is shown with the best fit (black). In the top panel, the different components are shown as dotted lines (continuum), red curves (broad-line components), blue curves (narrow-line components of Hα and a pair of [N II] lines). In the bottom panel, the fit of the Mg II line with Fe II emission (upper) and without Fe II emission (lower) are shown. The different components are indicated as red curves (individual broad-line components) and a green curve (Fe II emission component).

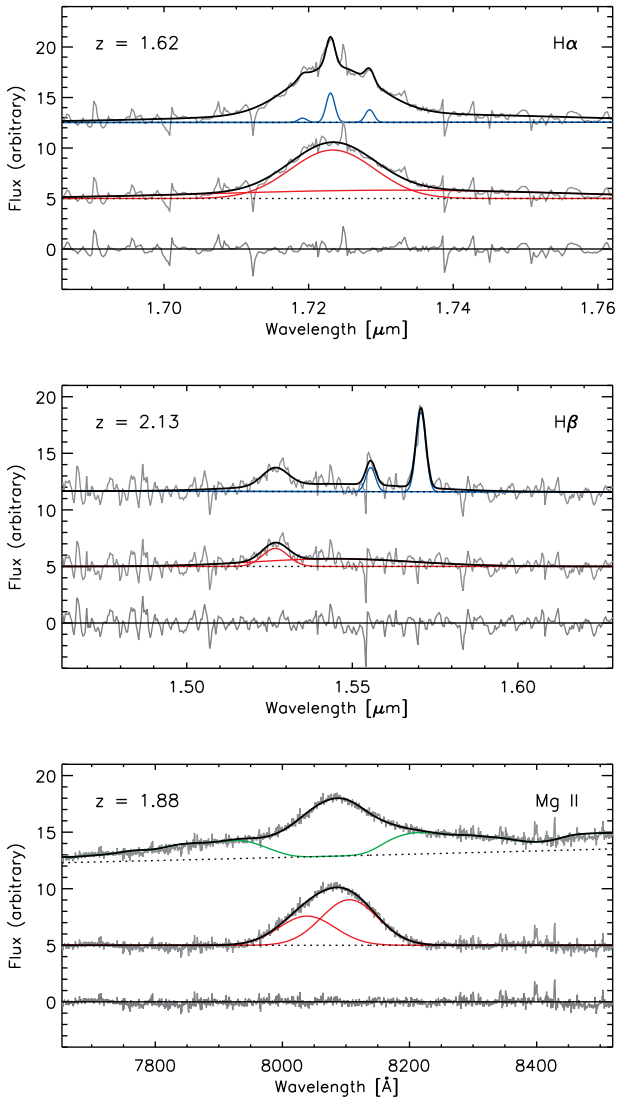

FIG. 3.— Examples of the broad-line fits for Hα (top), Hβ (middle), and Mg II (bottom) emission lines at $z = 1.62$, 2.13, and 1.88, respectively. The upper plot of each panel shows the observed spectrum (grey) with the best-fit model (black). The power-law continuum (dotted), narrow-line components (blue), and Fe II emission component (green) are also indicated, respectively. The middle plot of each panel shows the only broad-line components after subtraction of the best-fit model of continuum, narrow components and Fe II emission. The best-fit broad-line model is shown with the black curve. Each Gaussian broad-line component is also shown with red curves. The residual is shown in the lower plot of each panel.

Hα and a pair of [N II] lines), and green curve (Fe II emission). While it is uncertain whether the Mg II line is blended with Fe II emission or it really has a very broad-component in the bottom panel, we confirm that the Mg II line fit with Fe II emission is likely to show a similar result with Hα line fit in the upper panel.

In order to guarantee a reliable fit, we compare the fit with only narrow-line components, that with narrow-line and one broad Gaussian components, and that with narrow-line and two broad Gaussian components. We perform an F-test to decide whether an additional broad component is needed. We then subtract the narrow line components from the spectra obtaining a spectrum that contains only broad-line components. Finally, we inspect all fits by eye to check the cases where a broad component is unclear due to the low signal-to-noise ratio (S/N). We only consider spectra having S/N greater than 10 per pixel.

We determine the broad-line width and the line luminosity from the sum of the broad-line components. From the best-fit, the FWHM of the broad Hα, Hβ, and Mg II lines are computed and corrected for the effect of instrumental resolution to obtain an intrinsic velocity width. We select the broad-line AGNs with broad emission line widths larger than 2000 km/s of FWHM, a secure threshold for truly broadened lines, as compared to the spectral resolution. Additionally, we take into account the uncertainty in the derived FWHM and luminosity. We perform a Monte Carlo simulation comprising 100 realizations adding noise to each spectrum and iterate the whole procedure to find the best-fit model and the errors compatible with the observations, in order to assess the accuracy of the black hole mass measured. Since the best-fit model could have either one or two broad-line components during different Monte Carlo realizations for each spectrum, this could introduce a larger scatter.

In Figure 3, we show examples of broad-line fits for

Hα (top), Hβ (middle), and Mg II (bottom) emission lines at $z = 1.62$, 2.13, and 1.88, respectively. The upper plot of each panel shows the observed spectrum (grey) with the best-fit model (black). The power-law continuum (black dotted), narrow-line components (blue), and Fe II emission component (green) are also indicated, respectively. The middle plot of each panel shows the broad-line only components after subtraction of the best-fit model of continuum, narrow-line components and Fe II emission. The best-fit broad-line model is shown with the black curve. Each Gaussian broad-line component is also shown with red curves. The residual is shown in the lower plot of each panel.

5.2. *Black hole masses*

We calculate black hole masses from the FWHM and the luminosity of the sum of the broad line components. In the case of Hα and Hβ we use the recipes provided by Greene & Ho (2005). In addition, we specifically estimate the black hole mass based on the FWHM of the broad Mg II line and the monochromatic continuum luminosity at 3000Å using the calibration derived by the McLure & Dunlop (2004). The black hole mass can be expressed in the forms:

$$M_{BH} = 10^{6.301} \left(\frac{L_{H\alpha}}{10^{42}\ \mathrm{ergs\ s^{-1}}}\right)^{0.55} \left(\frac{FWHM_{H\alpha}}{10^{3}\ \mathrm{km\ s^{-1}}}\right)^{2.06}\ M_\odot \quad (1)$$

$$M_{BH} = 10^{6.556} \left(\frac{L_{H\beta}}{10^{42}\ \mathrm{ergs\ s^{-1}}}\right)^{0.56} \left(\frac{FWHM_{H\beta}}{10^{3}\ \mathrm{km\ s^{-1}}}\right)^{2.0}\ M_\odot \quad (2)$$

$$M_{BH} = 10^{0.505} \left(\frac{\lambda L_{\lambda 3000}}{10^{44}\ \mathrm{ergs\ s^{-1}}}\right)^{0.62} \left(\frac{FWHM_{MgII}}{\mathrm{km\ s^{-1}}}\right)^{2.0}\ M_\odot \quad (3)$$

where FWHM is the FWHM of the line in units of 1000 km/s, and $L_{\lambda 3000}$ is the continuum luminosity at 3000Å.

We present the comparison of black hole masses estimated using the Hα line with that using the Hβ (red square), or Mg II (red circles) lines in Figure 4, respectively. We also show the observations from Matsuoka et al. (2013) and Shen & Liu (2012) as grey and black open circles for comparison, respectively. The black dashed line denotes a one-to-one relation. Our sample of broad-line AGNs spans a range of $7.0 < \log M_{BH}/M_\odot < 9.5$ which is consistent with the previous studies of moderate-luminosity AGNs at $z \sim 1-2$ (Merloni et al. 2010; Trump et al. 2011; Matsuoka et al. 2013). The ratios of the mean black hole mass are $\log(M_{Mg\,II})/\log(M_{H\alpha})$=0.15, and $\log(M_{H\beta})/\log(M_{H\alpha}) = -0.27$, respectively. The median uncertainty of the black hole mass is ∼ 0.1 dex. While there are offsets between the different black hole mass estimations, it is worth noting that the black hole mass estimated with different calibrations carries a scatter of ∼ 0.3 dex (McGill et al. 2008). We also note that determination of black hole mass from the Hβ emission line are known to be affected by significant systematic uncertainties due to the Balmer decrement. If there are multiple lines measured, we use the lines in order of Hα, Mg II, and Hβ for the determination of the black hole mass. There are six objects in our sample that black hole masses are determined with the Hβ line.

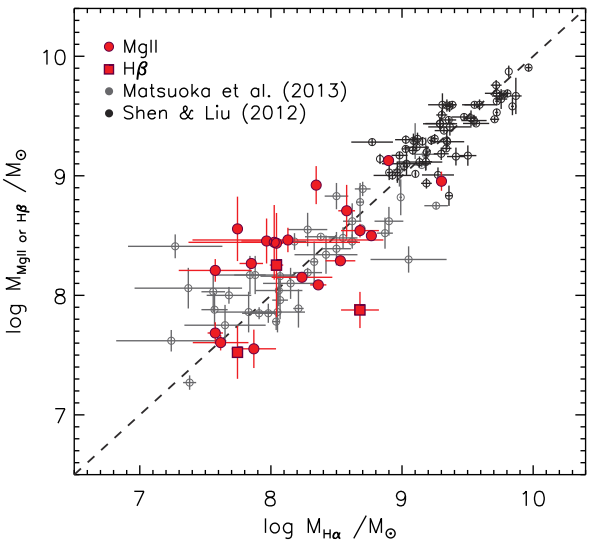

FIG. 4.— Comparison of black hole masses estimated using the Hα line with that using the Mg II line (red circles) or the Hβ line (red squares). Our sample of AGNs are shown in red, and the observations from Matsuoka et al. (2013) and Shen & Liu (2012) are also shown as grey and black symbols, respectively. The black dashed line denotes a one-to-one relation.

5.3. *Broad-line AGNs*

We select the sample of broad-line AGNs for which one or more broad emission lines have been identified in the spectrum. From the NIR/optical spectra, the Hα, Hβ, and Mg II wavelength regions are covered for 152, 56, and 62 spectra, respectively. Broad Hα, Hβ, and Mg II lines are detected for 52, 7, and 53 in the NIR and/or optical spectra, respectively, by broad-line widths larger than 2000 km/s of FWHM with the high S/N. For 19 AGNs, broad lines are detected in both Hα and Mg II lines (Figure 4). While all AGNs with detection of broad Hα lines are also detected in the broad Mg II line, 5 AGNs with broad Mg II line show no broad Hα line, mainly due to the low S/N NIR spectra. It is noted that there are quite a number clear broad Hα lines with practically absent Hβ lines, indicating a large Balmer decrement. The final sample of broad-line AGNs in the CDF-S, E-CDF-S, and *XMM*-LH fields consists of 86 objects.

6. EDDINGTON RATIO DISTRIBUTION

The mass accretion onto the black hole is important for a better understanding of the AGN evolution. The Eddington ratio, the ratio between the AGN bolometric luminosity and the Eddington luminosity (L_{bol}/L_{Edd}), provides insight into the black hole growth since the bolometric luminosity reflects the mass accretion rate. We show AGN bolometric luminosity versus black hole mass for our sample of broad-line AGNs in the different redshift bins in the left panel of Figure 5. The different X-ray surveys are shown with different symbols as labeled. The dotted reference lines indicate constant Eddington ratios of 1, 0.1, 0.01, and 0.001, respectively. Our sample of broad-line AGNs covers the black hole mass range $7.0 < \log M_{BH}/M_\odot < 9.5$ and the bolometric luminosity range $43 < \log L_{bol} < 47$ with a wide dispersion in the Eddington ratio distri-

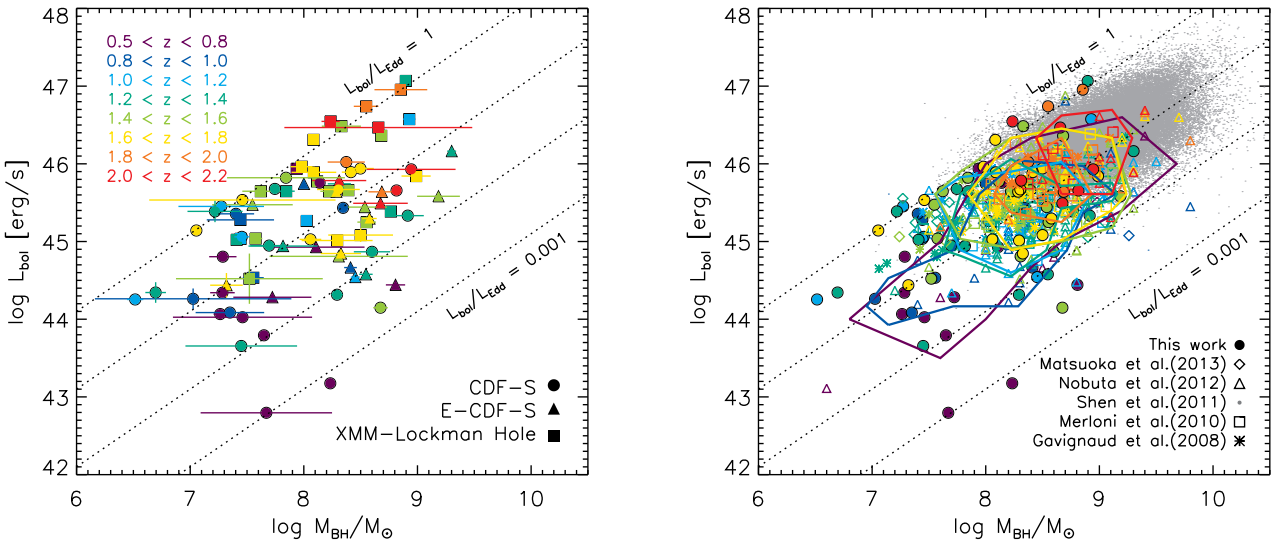

FIG. 5.— AGN bolometric luminosity versus black hole mass for our sample of broad-line AGNs in the different redshift bins (left). In the right panel, contours at the 1σ level are shown in the different redshift bins, together with the published observations from the literature as labeled. As a reference, lines of constant Eddington ratio (L_{bol}/L_{Edd}) equals to 1, 0.1, 0.01, and 0.001 are plotted as dotted lines.

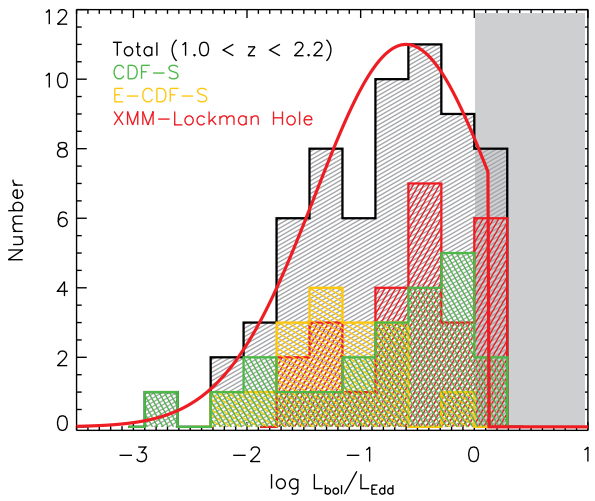

FIG. 6.— Eddington ratio distribution of broad-line AGNs at $1.0 < z < 2.2$. The different X-ray surveys are shown in different color histograms, and the black histogram represents the combined distribution of all surveys. The grey shade indicates the Eddington limit. The red solid line indicates a log-normal fit with a peak of $\log L_{bol}/L_{Edd} = -0.6$ and a dispersion of 0.8 dex.

bution. For comparison, we show published observations in the same redshift range from the literature in the right panel of Figure 5 (Gavignaud et al. 2008; Merloni et al. 2010; Shen et al. 2011; Nobuta et al. 2012; Matsuoka et al. 2013). The SDSS quasar sample (grey points; Shen et al. 2011) is limited to the high-mass and high-luminosity regime because the SDSS detection limit corresponds to a luminosity of $\log L_{bol} \sim 46$ at $z \sim 1$. Compared to the SDSS quasar sample, our sample of broad-line AGNs show a wider dispersion in the black hole mass, AGN bolometric luminosity and Eddington ratio distribution, consistent with previous studies on deep AGN sample (Gavignaud et al. 2008; Merloni et al. 2010; Nobuta et al. 2012; Matsuoka et al. 2013), which fill in the low-mass and low-luminosity region. The figure shows contours at the 1σ level, together with the literature data, except the SDSS quasar sample. The figure also reveals that only a small number of AGNs exceeds the Eddington limit by a small amount. AGNs with similar black hole masses show a broad range of bolometric luminosities spanning about two orders of magnitude, indicating that the accretion rate of black holes is widely distributed. This suggests that the AGN cosmic downsizing phenomenon could be explained by some more massive black holes with low accretion rates, which are relatively fainter than less massive black holes with efficient accretion. Lusso et al. (2012) suggest that AGNs show higher Eddington ratios at higher redshift at any given M_{BH}, and the Eddington ratio increases with bolometric luminosity. We confirm that there is a tendency for low-luminosity AGNs ($\log L_{bol} \lesssim 45.5$) with less massive black holes ($\log M_{BH}/M_{\odot} \lesssim 8$) to have lower Eddington ratios than high-luminosity AGNs ($\log L_{bol} \gtrsim 45.5$) with massive black holes ($\log M_{BH}/M_{\odot} \gtrsim 8$), consistent with Lusso et al. (2012). It is important to note that, when comparing with results in the literature, one should take into account the different methods of spectral line fitting and correction for bolometric luminosities. Nevertheless, they show similar distributions of the accretion rate of black holes over a wide range, consistent with previous studies.

Several studies have found a correlation between the X-ray bolometric correction and the Eddington ratio (e.g. Vasudevan & Fabian 2007; Lusso et al. 2012), which may introduce biases into this diagram. Lusso et al. (2012) found that there is a trend for higher bolometric corrections at higher bolometric luminosities. Vasudevan & Fabian (2007) suggest that there appears to be a distinct step change in bolometric correction at an Eddington ratio of ~ 0.1, below which apply lower bolometric corrections, and above which apply higher bolometric corrections. If one includes this correlation to the trend between bolometric luminosities and black

hole masses in Figure 5, which low-luminosity AGNs have lower accretion rates while high-luminosity AGNs show higher accretion rates, would even be more pronounced. However, we note the possibility that there could be the spurious correlations since L_{bol} is present on both axes when plotting the bolometric correction against the Eddington ratio.

We show the Eddington ratio distribution of our sample of AGNs in the redshift range $1.0 < z < 2.2$ in Figure 6. The different X-ray surveys are shown in different color histograms, and the black histogram represents the combined distribution of all surveys. The distribution of Eddington ratios peaks at $\log L_{bol}/L_{Edd} \sim -1$ with an extended tail towards low Eddington ratios, down to $\log L_{bol}/L_{Edd} \sim -3$. A log-normal fit with a peak of $\log L_{bol}/L_{Edd} = -0.6$ and a dispersion of 0.8 dex is shown as red solid line. In previous studies, Kollmeier et al. (2006) suggest that the Eddington ratios are quite narrowly distributed independent of luminosity ($L_{bol} = 10^{45} - 10^{47}$ erg/s) and redshift ($0.3 < z < 4.0$), with a dispersion of 0.3 dex (see also Steinhardt & Elvis 2010). Lusso et al. (2012) also suggest that the distribution of Eddington ratios are nearly Gaussian especially at high-redshift and at high L_{bol}/M_{BH}, with a dispersion of ∼0.35 dex, while the low-redshift and low L_{bol}/M_{BH} are more affected by incompleteness. We list our sample of broad-line AGNs in Appendix Table 3, which includes AGN bolometric luminosities, black hole masses, and measurements of emission line properties.

We should emphasize here that the systematic selection effects could certainly be playing a role in determining the distribution of AGN bolometric luminosities and black hole masses. The Eddington ratio distribution, thus, could be a result of the selection bias, mainly the limited X-ray luminosity but also to the broad line width, i.e. the black hole mass. The X-ray luminosity is limited by the X-ray flux limit, depending on redshift and on the limited volume. The detectability of the broad emission line gives rise to a bias against the black hole mass. Also, the black hole mass could be biased by observational limitations to detect the corresponding very broad lines and low signal-to-noise spectra. This is bound to introduce selection biases, which could mimic artificial correlations in the data. Hence, we will further discuss the possible selection effects in the next section.

7. ANALYSIS OF SELECTION BIASES

We investigate the possible bias due to systematics and selection effects on the observed AGN bolometric luminosity and the black hole mass. To explore the effect of these selection biases, we construct Monte Carlo simulations to make artificial datasets, which are affected by the same selection effects. We start from the bolometric luminosity function of AGNs (Hopkins et al. 2007) in the different redshift bins with an assumption for the Eddington ratio distribution, which has a peak of $\log L_{bol}/L_{Edd} = -0.6$ and a dispersion of 0.8 dex, bounded by L_{Edd}, taken from the observed distribution (see red curve in the top panel of Figure 6). To account for the observed selection biases, we apply the same selection effects based on our combined X-ray surveys. The X-ray flux limit corresponds to a bolometric luminosity of $\log L_{bol} \sim 43$ at $z \sim 1$. We use the survey area of the total combined X-ray surveys (black curve in the right panel of Figure 1). Since it has been known that there is much larger fraction of obscured AGN at lower luminosities (Ueda et al. 2003; Steffen et al. 2003; Simpson 2005; Hasinger 2008), we apply the fraction of broad-line AGNs as a function of AGN luminosity from Hasinger (2008), to which the same bolometric correction (Marconi et al. 2004) was applied to the X-ray luminosity. The black hole mass is biased by the detectability of the broad emission line and the signal-to-noise of spectra. We, thus, apply a 'fudge' factor, which is the exponentially decaying function at low-mass ($6.5 < \log M_{BH} < 7.5$) and high-mass ($8.5 < \log M_{BH} < 9.5$). The 'fudge' factor brings down the numbers of low-mass ($6.5 < \log M_{BH} < 7.5$) and high-mass ($8.5 < \log M_{BH} < 9.5$) AGNs, which takes into account the spectroscopic incompleteness. For each data set of the different redshift bins, we calculate black hole masses from the AGN bolometric luminosity and the Eddington ratio. The Eddington ratio distribution is assumed to be same regardless of AGN luminosity or redshift, which is a valid assumption for the high-luminosity AGNs (Kollmeier et al. 2006). Steinhardt & Elvis (2010) report that the Eddington ratio distributions are all similar for SDSS quasar populations over a wide range of mass and redshift.

In Figure 7, the Monte Carlo simulated data sets (left panel), and those which are affected by the same observed selection effects (right panel) are shown with grey symbols and contours at the 1σ level in the different redshift bins. The black solid line in the right panel of Figure 7 indicates the assumed peak of Eddington ratio, $\log L_{bol}/L_{Edd} = -0.6$. The AGN downsizing trend is seen in the sense that the characteristic AGN luminosity and black hole mass decrease with redshift. This is primarily due to the strong evolution of the co-moving number density at the bright end of the AGN luminosity function at $0.5 < z < 2.0$, together with the corresponding selection biases. We compare the simulated data with the observed AGNs in the different redshift bins in Figure 8. The simulated data sets are shown in grey with the contour at the 1σ level, and the observed AGNs are shown in colored symbols for each redshift bin in the top panels. For each redshift bin we group the data into four sets, using a constant Eddington ratio of $L_{bol}/L_{Edd} = 0.1$ and a line perpendicular to the Eddington ratio as separation. In the bottom panels, the number of detected (observed) sources over the number of expected (simulated) sources is given in parentheses, as well as the Poisson likelihood calculated from this combination. In bins of high-luminosity AGNs with high Eddington ratio as well as low-luminosity AGNs with low Eddington ratio the detected number of objects agrees with the prediction from the Monte Carlo simulation within the statistical errors. However, for low-luminosity AGNs with high Eddington ratios, especially at high redshift ($1.8 < z < 2.2$) and low redshift ($0.5 < z < 0.8$) bins, the simulations systematically predict a larger number of objects, than those observed. Taking all Poisson likelihoods together, there is a difference between the observed and the predicted distributions. We therefore suggest that there is a dependence of AGN luminosities on the Eddington ratios in the sense that luminous AGNs appear to have systematically higher Eddington ratios than low-luminosity AGNs. However, this result is of marginal significance due to the relatively small number of objects in each bin. We note

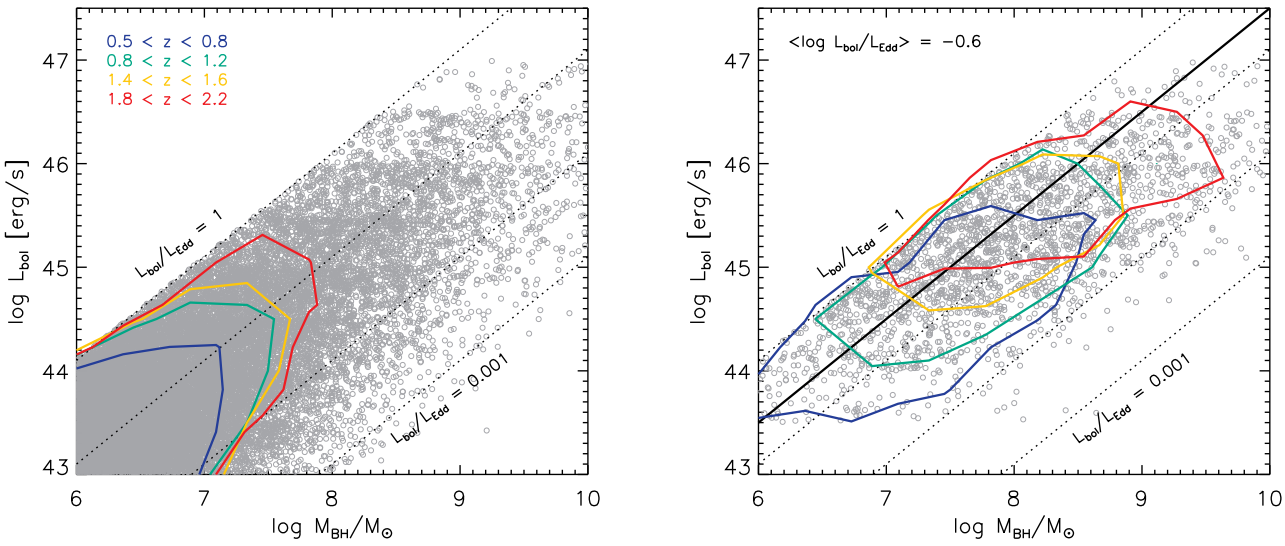

FIG. 7.— Monte Carlo simulated data sets from the AGN bolometric luminosity function (Hopkins et al. 2007) in the different redshift bins with an assumption for the Eddington ratio distribution, which has a peak of log $L_{bol}/L_{Edd} = -0.6$ and a dispersion of 0.8 dex (red curve in Figure 6) regardless of AGN luminosity or redshift. The simulated data sets (left), and those which are affected by the same observed selection effects (right) are shown in grey. As a reference, lines of constant Eddington ratio (L_{bol}/L_{Edd}) equals to 1, 0.1, 0.01, 0.001 are plotted as dotted lines. Contours at the 1σ level are shown in the different redshift bins. The black solid line indicates the assumed peak of Eddington ratio.

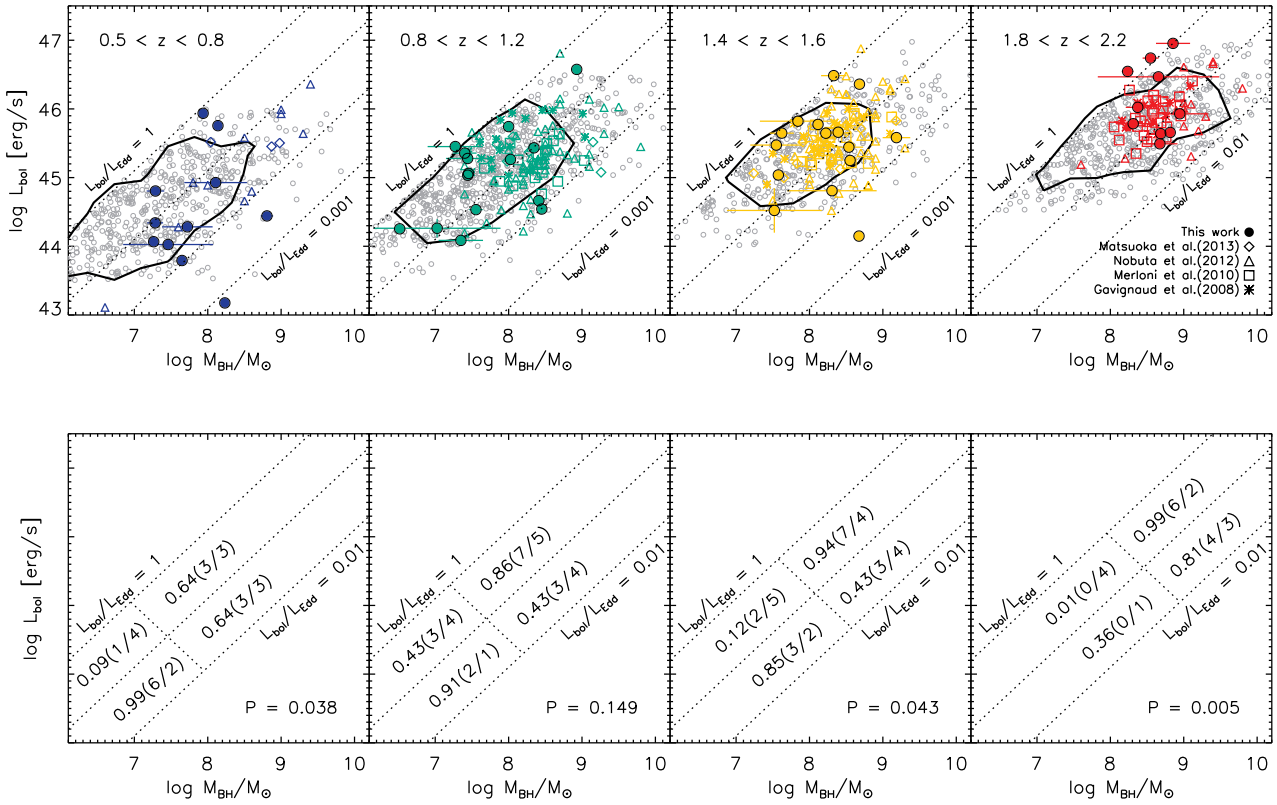

FIG. 8.— Comparison of the Monte Carlo simulated data sets with the observed AGNs in the different redshift bins. In the top panels, the simulated data sets are shown in grey with the 1σ contour, and the observed AGNs are shown as purple ($0.5 < z < 0.8$), green ($0.8 < z < 1.2$), yellow ($1.4 < z < 1.6$), and red ($1.8 < z < 2.2$) symbols, respectively. In the bottom panels, the Poisson likelihood is shown in each bin, which is perpendicular to the Eddington ratio plane. The numbers in parentheses refer to detected (observed) sources over expected (simulated) sources. Reference lines of constant Eddington ratios are plotted as dotted lines.

that our sample of high-luminosity X-ray selected AGNs overlaps with the less luminous quasars from the SDSS sample at the highest Eddington ratios (see grey points in the right panel of Figure 5), while the most luminous, most massive SDSS quasars lie further away from their Eddington luminosity (Steinhardt & Elvis 2010).

8. DISCUSSION

We now discuss the observed AGN downsizing phenomenon, and possible explanations for the black hole growth over cosmic time. The decrease of the characteristic luminosity of AGNs with redshift has been described as AGN downsizing, implying that the AGN activity at earlier epochs was much more intense. We show that AGNs with similar black hole masses show a broad range of bolometric luminosities, which means the accretion rate of black holes is widely distributed. The average accretion rate of two different AGN fueling mechanisms can play a crucial role for the downsizing interpretation. AGN activity triggered by major mergers is thought to have a higher accretion rate than activity triggered by secular evolution effects. Therefore the luminosity of an AGN with a certain black hole mass may differ widely, depending on the accretion mechanisms.

The colors and morphologies of galaxies may contain a record of their growth history. Several studies have addressed that the majority of AGN host galaxies in the local universe are preferentially in the "green valley" on the color-magnitude diagram, between actively star-forming galaxies in the blue cloud and passively evolving galaxies on the red sequence (e.g. Schawinski et al. 2010). Moreover, a large fraction of moderate-luminosity AGNs are likely to live in disk-dominated galaxies (Gabor et al. 2009; Cisternas et al. 2011; Schawinski et al. 2011; Kocevski et al. 2012; Mullaney et al. 2012; Rosario et al. 2015). Fan et al. (2014) find that the majority of AGN host galaxies show no significant merger features up to $z \sim 2$. It is likely that merger features are visible only for a few Gyrs after major mergers (e.g. Lotz et al. 2008; Ji et al. 2014), suggesting that most AGN activity does not seem to be triggered by major mergers since $z \sim 2$ (see also Mainieri et al. 2011; Silverman et al. 2011; Schawinski et al. 2012; Schramm & Silverman 2013; Villforth et al. 2014). Allevato et al. (2011) further point out that moderate-luminosity AGNs at $z = 0 - 2$ live in relatively massive dark matter halos ($10^{13.5} M_{\odot}$), which corresponds to rich groups of galaxies, independent of redshift. The rich group environment may provide a kind of "goldilocks" zone for AGNs in the sense that on one hand the density is high enough to cause frequent gravitational disturbances bringing cold gas to the center, and on the other hand the gas density in the group is not high enough to remove the cold gas from the galaxies due to ram pressure stripping. This also indicates that major mergers cannot be the main driver of the late evolution of AGNs. This raises interesting questions regarding different fueling mechanisms for the growth of black holes and galaxies at different epochs during cosmic time.

Given these intriguing findings, a possible interpretation for explaining the cosmic downsizing as well as morphologies and colors of AGN host galaxies is that there are two different modes of AGN feedback at different epochs (see Hasinger 2008). In an active AGN phase at high redshift, black holes have experienced vigorous growth by major mergers while radiating close to the Eddington limit (see e.g. Di Matteo et al. 2005). When they reach a critical mass, at which the AGN is sufficient to blow out the surrounding gas, the feedback of the black hole suppresses further star formation and creates a red bulge-dominated remnant (e.g. Fabian 1999; Springel et al. 2005). It is likely that only a small fraction of the transient population can be found in between the blue cloud and the red sequence due to rather short merger timescale ($\sim 10^8$ yrs). The relatively massive galaxies, which have already experienced substantial growth by previous mergers, grow slowly through episodic star formation via secular evolution, leading to a disc surrounding the bulge. The modest AGN activity can be triggered by the gas accretion over cosmic time via internal, secular processes, such as gravitational instabilities in the disc. This secular growth is slow enough, and thus, the presence of AGN host galaxies in the green valley on the color-magnitude diagram could be interpreted as evidence for the on-going star formation in the inner region of low-luminosity AGN host galaxies at lower redshift, coming down from the red sequence. This is also compatible to the weak link between merger features and the AGN activity, as well as the moderate-luminosity AGNs in the relatively massive dark matter halos at $z \lesssim 2$, where the number density of most luminous AGNs starts to decline. Finally, the late feedback from AGNs suppresses the late cooling flows of hot gas, keeping the galaxy quiescent. This seems to consistent with dormant supermassive black holes in dynamically hot systems (e.g. massive early-type galaxies) that contain little cold gas and correspondingly little star-formation. All of these seem to be consistent with the hierarchical growth scenario.

9. SUMMARY

We present the Eddington ratio distribution of X-ray selected broad-line AGNs in the CDF-S, E-CDF-S, and the *XMM*-LH surveys. We calculate AGN bolometric luminosities from absorption-corrected X-ray luminosities, and estimate black hole masses of broad-line AGNs using the optical and Subaru/FMOS near-infrared spectroscopy. Our sample of broad-line AGNs spans the bolometric luminosity range $L_{bol} \sim 10^{43.5-47}$ erg/s, and the black hole mass range $M_{BH} \sim 10^{6.5-9.5}$ $M_{\odot}$ with a broad range of Eddington ratios $L_{bol}/L_{Edd} \sim 0.001 - 1$.

We explore the systematics and selection biases, because in general observed distributions are dependent on the X-ray flux limit and the detectability of the broad emission lines. Based on the analysis on these effects, we find that the observed downsizing trend could be simply explained by the strong evolution of the co-moving number density at the bright end of the AGN luminosity function at $0.5 < z < 2.0$, together with the corresponding selection effects. However, in order to explain the relatively small fraction of low-luminosity AGNs with high accretion rates, we might need to consider a correlation between the AGN luminosity and the accretion rate of black holes that luminous AGNs have higher Eddington ratios than low-luminosity AGNs. We suggest that the AGN downsizing trend can be interpreted as the fraction of AGNs radiating close to the Eddington limit decrease after their peak activity phases, suggesting that the fu-

eling mechanism of growth of black holes might change through the cosmic time.

We thank the anonymous referee for several comments, which helped to improve the quality of the manuscript significantly. We thank Amy Barger for useful comments that helped improve this paper.

Facilities: Subaru (FMOS)

APPENDIX

SUBARU/FMOS SPECTROSCOPIC OBSERVATIONS

In Table 2, we present the identified spectroscopic redshifts from the Subaru/FMOS observations. The ID is from the published catalog of CDF-S (Xue et al. 2011), E-CDF-S (Lehmer et al. 2005), and *XMM*-LH (Brunner et al. 2008). We assign a quality flag that gives the confidence in the redshift measurement. Flag 2 indicates a reliable redshift due to high signal-to-noise ratio (S/N) spectra and multiple spectral features. Flag 1 indicates that a redshift is not securely identified due to either low S/N or the presence of only a single emission line with no additional features. The newly discovered spectroscopic redshifts are marked with a cross sign. "++" if no previous spectroscopic redshift and "+" if the previous spectroscopic redshift is insecure. The redshift column gives our best redshift estimate. We also present the previous spectroscopic and photometric redshifts from the catalog.

In Table 3, we list our sample of broad-line AGNs, which includes AGN bolometric luminosities, black hole masses, and measurements of emission line properties.

TABLE 2 Subaru/FMOS spectroscopic observations

Field	ID	RA	Dec	Redshift	Quality	z_{spec}	z_{phot}	Band	Emission features
CDF-S	1	52.899	-27.860	1.630	2+	1.624	1.626	J-long, H-long	Hβ, Hα, [N II], [S II]
CDF-S	4	52.930	-27.901	1.270	2+	1.271	1.027	J-long, H-short, H-long	Hα, [S II]
CDF-S	7	52.936	-27.865	0.880	1++	-99.0	0.881	H-long	[S II]
CDF-S	25	52.960	-27.870	1.336	2	1.374	1.386	H-short	Hα, [S II]
CDF-S	26	52.960	-27.864	1.447	1++	-99.0	1.438	J-long, H-short, H-long	Hβ
CDF-S	31	52.963	-27.744	1.608	2++	-99.0	1.829	H-short, H-long	Hα, [N II], [S II]
CDF-S	36	52.967	-27.804	1.236	1+	1.236	1.223	H-short	Hα, [N II]
CDF-S	37	52.968	-27.696	1.020	2+	0.857	1.021	J-long	Hα, [N II]
CDF-S	49	52.980	-27.841	1.212	1+	1.212	1.208	H-short	[N II], [S II]
CDF-S	51	52.981	-27.913	0.726	2	0.737	0.724	J-long	Hα, [S II]
CDF-S	54	52.983	-27.823	1.219	2++	-99.0	1.208	H-short	Hα, [N II]
CDF-S	64	52.991	-27.793	0.856	1++	-99.0	-99.0	J-long, H-long	Hα
CDF-S	67	52.993	-27.845	1.544	2++	-99.0	3.309	J-long, H-long	Hα
CDF-S	72	52.998	-27.839	1.638	1+	1.574	1.900	J-long, H-long	Hα
CDF-S	76	53.002	-27.722	1.042	2	1.037	1.05	J-long, H-long	Hα, [N II]
CDF-S	80	53.003	-27.893	1.549	2++	-99.0	1.593	J-long, H-short, H-long	Hα, [N II]
CDF-S	81	53.004	-27.799	0.975	2	0.975	0.951	J-long	Hα, [N II], [S II]
CDF-S	83	53.006	-27.780	1.307	2++	-99.0	1.499	H-short, H-long	Hα
CDF-S	84	53.006	-27.694	1.414	1	1.406	1.379	H-short	Hα, [N II]
CDF-S	88	53.010	-27.767	1.613	1	1.616	1.626	J-long, H-long	Hβ, Hα
CDF-S	99	53.016	-27.891	3.039	1++	-99.0	3.877	H-short	[O II]
CDF-S	101	53.017	-27.624	0.966	2	0.977	1.000	J-long	Hα
CDF-S	109	53.020	-27.691	1.524	2+	0.720	1.562	J-long, H-long	Hβ, [O III]
CDF-S	112	53.023	-27.757	1.189	1+	1.189	1.129	H-short	Hα, [N II]
CDF-S	113	53.024	-27.746	1.609	1+	1.608	1.692	J-long, H-long	[O II], Hα
CDF-S	117	53.025	-27.824	1.295	1++	-99.0	1.208	J-long, H-short, H-long	Hα
CDF-S	118	53.026	-27.673	1.624	2++	-99.0	1.438	H-long	Hα, [N II]
CDF-S	120	53.027	-27.791	1.021	2	1.021	1.023	J-long	Hα, [N II]
CDF-S	121	53.027	-27.765	1.329	1	1.329	1.321	H-short	Hα, [N II]
CDF-S	127	53.029	-27.936	0.774	2	0.777	0.767	J-long, H-long	Hα, [N II], [S II], [S III]
CDF-S	131	53.031	-27.856	1.546	1+	0.034	1.546	J-long, H-long	[O III], Hα
CDF-S	135	53.033	-27.626	0.977	1	0.976	1.000	J-long, H-short, H-long	Hα, [N II]
CDF-S	143	53.036	-27.850	0.736	2	0.736	0.718	J-long	Hα, [N II]
CDF-S	152	53.041	-27.887	0.740	1	0.743	0.750	J-long	Hα, [S II]
CDF-S	165	53.046	-27.729	0.998	2	0.998	1.000	J-long	Hα, [N II]
CDF-S	166	53.046	-27.738	1.611	1	1.605	1.626	J-long, H-long	Hα, [N II]
CDF-S	182	53.052	-27.820	1.048	2+	1.048	0.904	J-long	Hα
CDF-S	205	53.060	-27.853	1.540	2	1.544	1.562	J-long, H-long	[O III], Hα, [N II]
CDF-S	222	53.066	-27.702	1.691	1++	-99.0	2.779	H-long	Hα
CDF-S	226	53.067	-27.817	1.412	1	1.413	1.438	H-short	Hα
CDF-S	229	53.068	-27.658	1.326	2	1.324	1.321	J-long, H-short	Hβ, [O III], Hα, [N II], [S II]
CDF-S	236	53.071	-27.834	1.613	2	1.611	1.579	J-long, H-long	Hα, [S II]
CDF-S	257	53.076	-27.849	1.535	2	1.536	1.562	H-long	Hα
CDF-S	271	53.081	-27.681	0.681	1	0.761	0.709	H-short	[S III]
CDF-S	290	53.087	-27.930	2.301	2++	-99.0	2.826	H-short	Hγ
CDF-S	308	53.094	-27.768	1.729	1	1.735	1.264	J-long, H-long	[O III], Hα
CDF-S	329	53.102	-27.670	0.954	2++	-99.0	1.050	J-long	Hα, [N II]
CDF-S	344	53.105	-27.705	1.615	2	1.617	1.626	J-long, H-long	[O III], Hα, [N II], [S II]
CDF-S	349	53.106	-27.772	0.896	2	0.896	0.904	J-long	Hα, [N II]
CDF-S	368	53.111	-27.824	1.469	2	1.468	1.560	J-long, H-long	[O III], Hα, [S II]
CDF-S	369	53.111	-27.670	1.612	2	2.208	2.202	J-long, H-long	Hβ, Hα, [N II], [S II]
CDF-S	405	53.123	-27.723	1.614	2+	1.609	1.598	J-long, H-short, H-long	Hα, [N II]

TABLE2 – continued.

Field	ID	RA	Dec	Redshift	Quality	z_{spec}	z_{phot}	Band	Emission features
CDF-S	409	53.124	-27.863	1.316	2+	1.316	5.247	H-short	Hα
CDF-S	414	53.124	-27.756	0.953	2	0.953	0.951	J-long	Hα
CDF-S	415	53.125	-27.717	1.357	2	1.356	1.328	H-short	Hα, [N II], [S II]
CDF-S	417	53.125	-27.758	1.222	2	1.209	1.208	H-short	Hα, [N II], [S II]
CDF-S	420	53.125	-27.756	0.960	2	0.960	0.951	J-long	Hα, [N II], [S II]
CDF-S	424	53.126	-28.005	2.310	2	2.306	2.282	J-long, H-long	[O III]
CDF-S	429	53.130	-27.655	1.040	1+	1.038	1.438	J-long, H-long	Hα, [N II]
CDF-S	436	53.131	-27.841	1.549	1+	1.613	1.485	J-long, H-long	Hα, [N II]
CDF-S	439	53.132	-27.833	0.980	1	0.98	0.983	J-long	Hα
CDF-S	467	53.142	-27.841	1.384	2	1.384	1.395	H-short	Hα
CDF-S	473	53.144	-27.654	1.557	2	1.510	1.499	H-long	Hα, [N II], [S II]
CDF-S	487	53.147	-27.667	1.473	1++	-99.0	1.490	J-long, H-short, H-long	Hα
CDF-S	491	53.149	-27.792	1.223	1	1.223	1.208	H-short	[S II]
CDF-S	492	53.149	-27.683	0.735	2	0.735	0.724	J-long	Hα, [N II], [S II]
CDF-S	499	53.151	-27.857	1.614	2	1.613	1.626	H-long	Hα
CDF-S	503	53.151	-27.713	1.542	2+	1.609	1.582	J-long, H-long	Hα, [N II], [S II]
CDF-S	518	53.157	-27.870	1.611	2	1.603	1.692	J-long, H-long	[O III], Hα, [N II], [S II]
CDF-S	519	53.158	-27.704	1.791	1+	1.814	-99.0	J-long, H-long	Hγ
CDF-S	524	53.160	-27.931	2.043	1++	-99.0	1.829	J-long, H-short, H-long	[O III]
CDF-S	557	53.171	-27.741	1.299	1	1.298	1.142	H-short	Hα, [N II]
CDF-S	580	53.181	-27.783	1.571	1+	1.570	1.578	J-long, H-long	Hβ, Hα, [N II]
CDF-S	586	53.184	-27.793	0.738	2	0.738	0.724	J-long	Hα
CDF-S	599	53.188	-27.904	1.380	1	1.378	1.328	H-short	Hα, [N II]
CDF-S	612	53.192	-27.891	1.381	1+	1.382	1.428	H-short	Hα, [N II], [S II]
CDF-S	619	53.196	-27.730	1.212	1	1.178	1.154	H-short	Hα, [N II]
CDF-S	623	53.197	-27.713	0.732	1	0.729	-99.0	J-long, H-long	Hα, [S II]
CDF-S	626	53.200	-27.709	0.979	2	0.979	1.000	J-long, H-long	Hα, [N II], [S II]
CDF-S	629	53.201	-27.882	0.660	1	0.667	0.601	H-short	[S III]
CDF-S	634	53.205	-27.681	1.226	2	1.222	1.208	J-long, H-short	Hα, [N II]
CDF-S	648	53.214	-27.929	1.448	2++	0.853	0.857	J-long, H-short, H-long	[S II]
CDF-S	652	53.216	-27.708	1.023	2	1.020	1.000	J-long	Hα, [N II]
CDF-S	656	53.218	-27.762	1.367	2	1.367	1.379	H-short	Hα, [N II], [S II]
CDF-S	661	53.226	-27.818	0.987	1+	0.988	0.999	J-long	Hα
CDF-S	680	53.246	-27.861	1.502	2++	-99.0	1.379	J-long, H-short, H-long	Hα, [N II], [S II]
CDF-S	683	53.247	-27.816	1.613	2++	-99.0	2.202	J-long, H-long	Hα, [N II]
CDF-S	698	53.261	-27.806	2.549	1++	-99.0	3.101	H-long	Hβ
CDF-S	699	53.261	-27.760	1.257	2+	1.130	1.301	H-short	Hα, [N II], [S II]
CDF-S	706	53.266	-27.841	0.891	2	0.891	0.904	J-long	Hα, [N II], [S II]
CDF-S	720	53.282	-27.858	1.609	1	1.609	2.535	J-long, H-long	[O III], Hα
CDF-S	724	53.287	-27.694	1.337	2	1.335	1.321	H-short	Hα, [S II]
CDF-S	728	53.292	-27.812	1.013	2	1.034	1.050	J-long, H-long	Hα, [N II]
CDF-S	731	53.302	-27.776	0.610	1++	-99.0	0.562	J-long, H-short, H-long	[S II]
E-CDF-S	61	52.870	-27.983	0.752	2	0.752	0.763	J-long	Hα
E-CDF-S	68	52.878	-27.976	1.362	1	1.366	1.382	H-short	Hα, [N II]
E-CDF-S	85	52.889	-27.805	0.822	1	0.678	0.669	J-long, H-short	Hα
E-CDF-S	89	52.891	-27.767	1.613	2++	-99.0	1.889	J-long, H-long	Hα, [N II]
E-CDF-S	105	52.904	-27.969	1.606	1++	-99.0	1.368	J-long, H-short, H-long	[O III], Hα, [S II]
E-CDF-S	115	52.911	-27.996	1.190	2++	-99.0	1.255	J-long, H-short, H-long	Hα, [N II]
E-CDF-S	118	52.916	-27.699	0.469	2	0.467	-99.0	J-long	[S II]
E-CDF-S	121	52.917	-27.940	5.137	2++	-99.0	5.315	J-long, H-long	Mg II
E-CDF-S	137	52.930	-28.020	1.197	2++	-99.0	1.425	J-long, H-short, H-long	Hα, [N II], [S II]
E-CDF-S	150	52.935	-27.943	0.727	2++	-99.0	0.879	J-long, H-long	Hα, [S III]
E-CDF-S	157	52.942	-27.695	1.322	2+	1.315	1.184	H-short	Hα, [N II]
E-CDF-S	166	52.947	-27.920	1.408	2	1.404	1.186	H-short	Hα, [N II]
E-CDF-S	193	52.963	-27.954	1.161	1	1.167	1.153	H-short	Hα, [N II]
E-CDF-S	195	52.963	-27.982	1.361	1	1.368	0.831	H-short	Hα, [N II]
E-CDF-S	201	52.966	-27.947	1.618	2++	-99.0	1.411	J-long, H-short, H-long	[O III], Hα
E-CDF-S	217	52.975	-28.046	1.602	2++	-99.0	1.578	J-long, H-long	[O II], [O III], Hα, [N II]
E-CDF-S	218	52.976	-27.997	0.738	1	0.740	0.731	J-long	Hα, [S II]
E-CDF-S	222	52.978	-28.017	0.662	2+	0.623	0.677	H-short	[S III]
E-CDF-S	234	52.987	-28.080	1.675	1++	-99.0	-99.0	J-long, H-short, H-long	Hα
E-CDF-S	235	52.987	-28.030	1.386	2	1.380	1.889	H-short	Hα, [N II]
E-CDF-S	276	53.018	-28.075	1.295	2++	-99.0	-99.0	J-long, H-short, H-long	[O III], Hα, [N II]
E-CDF-S	282	53.022	-28.071	1.215	2++	-99.0	-99.0	H-short	Hα, [N II]
E-CDF-S	298	53.029	-27.971	0.847	1++	-99.0	1.067	J-long, H-long	[S III]
E-CDF-S	342	53.066	-28.025	1.641	2++	-99.0	1.651	H-long	Hα
E-CDF-S	358	53.085	-28.037	1.626	2	1.624	1.635	J-long, H-long	Hβ, [O III], Hα, [N II], [S II]
E-CDF-S	372	53.108	-28.013	2.216	2++	-99.0	2.052	J-long, H-short, H-long	Hβ
E-CDF-S	384	53.116	-28.079	1.531	1++	-99.0	-99.0	J-long, H-short, H-long	Hα
E-CDF-S	388	53.122	-28.029	1.555	2+	0.638	1.591	J-long, H-short, H-long	Hα, [N II], [S II]
E-CDF-S	400	53.135	-28.058	1.222	2	1.220	1.102	J-long, H-short, H-long	Hα, [N II]
E-CDF-S	411	53.151	-27.589	1.226	2	1.220	1.199	J-long, H-short	Hα, [N II]
E-CDF-S	424	53.165	-28.014	1.517	2++	-99.0	1.507	J-long, H-short, H-long	Hα, [N II]
E-CDF-S	459	53.194	-27.995	1.667	1++	-99.0	-99.0	J-long, H-short, H-long	Hα
E-CDF-S	470	53.205	-28.063	0.680	1	0.680	0.644	J-long, H-short, H-long	[S III]
E-CDF-S	481	53.213	-28.034	2.529	1++	-99.0	2.695	J-long, H-short, H-long	[O III]
E-CDF-S	517	53.247	-27.603	1.345	2	1.350	1.337	H-short	Hα

TABLE2 – continued.

Field	ID	RA	Dec	Redshift	Quality	z_{spec}	z_{phot}	Band	Emission features
E-CDF-S	521	53.248	-27.624	1.608	1++	-99.0	1.484	J-long, H-long	Hα
E-CDF-S	538	53.256	-28.048	1.373	2+	0.200	1.812	J-long, H-short, H-long	Hα, [N II], [S II]
E-CDF-S	546	53.264	-27.885	0.892	1+	1.346	0.954	J-long, H-short	Hα, [S II]
E-CDF-S	557	53.271	-27.674	0.311	2	0.311	0.285	J-long, H-short, H-long	[S III]
E-CDF-S	571	53.278	-27.774	1.705	2	1.705	1.497	J-long, H-long	Hα, [N II]
E-CDF-S	588	53.287	-27.974	2.579	2	2.583	1.104	H-long	[O III]
E-CDF-S	595	53.290	-27.736	1.037	1++	-99.0	1.016	J-long, H-long	Hα, [N II]
E-CDF-S	601	53.294	-27.963	1.598	2	1.598	1.726	J-long, H-long	Hα, [N II], [S II]
E-CDF-S	621	53.310	-27.975	1.320	2++	-99.0	1.555	J-long, H-short, H-long	[O III], Hα, [N II]
E-CDF-S	624	53.311	-27.706	1.320	1++	-99.0	1.440	J-long, H-short, H-long	Hα
E-CDF-S	635	53.319	-27.952	1.045	2+	1.044	1.020	J-long	Hα
E-CDF-S	678	53.345	-27.923	1.629	2	1.628	1.633	J-long, H-long	Hβ, [O III], Hα, [N II]
E-CDF-S	681	53.347	-27.771	0.834	2	0.835	0.809	J-long	Hα
E-CDF-S	688	53.349	-27.725	0.787	2	0.787	0.786	J-long	Hα, [N II]
E-CDF-S	698	53.357	-27.816	1.413	1++	-99.0	1.464	J-long, H-short, H-long	Hα, [N II]
E-CDF-S	701	53.360	-27.722	0.964	2	0.964	0.950	J-long	Hα, [N II]
E-CDF-S	705	53.362	-27.755	1.658	1++	-99.0	1.835	H-long	Hα, [N II], [S II]
E-CDF-S	709	53.368	-27.972	1.558	1++	-99.0	-99.0	J-long, H-short	[O III]
E-CDF-S	715	53.371	-27.732	1.280	1++	-99.0	-99.0	J-long, H-short	Hα
E-CDF-S	716	53.372	-27.991	0.763	2	0.763	0.768	J-long	Hα, [N II], [S II]
E-CDF-S	718	53.374	-27.852	0.946	1	0.951	0.956	H-short, H-long	[S II]
E-CDF-S	725	53.383	-27.903	1.314	2	1.315	-99.0	J-long, H-short, H-long	Hα, [N II]
E-CDF-S	728	53.387	-27.819	1.583	2	1.581	1.568	J-long, H-short, H-long	Hα, [N II], [S II]
XMM-LH	5	163.180	57.263	2.138	2	2.144	2.050	H-short, H-long	Hβ, [O III]
XMM-LH	15	163.184	57.286	2.010	1++	-99.0	2.022	H-short	[O III]
XMM-LH	19	163.240	57.292	0.746	2++	-99.0	0.730	H-short, H-long	[S III]
XMM-LH	25	163.348	57.293	1.599	2++	-99.0	1.450	H-short, H-long	Hα, [N II]
XMM-LH	34	163.253	57.303	0.517	2++	-99.0	0.520	H-long	He I
XMM-LH	35	163.470	57.304	1.727	2++	-99.0	1.441	H-short, H-long	Hα, [N II]
XMM-LH	48	163.250	57.317	1.458	1++	-99.0	1.460	H-short, H-long	Hα
XMM-LH	50	163.107	57.318	4.470	2	4.449	4.340	J-long, H-short, H-long	Mg II
XMM-LH	51	163.032	57.318	2.677	1++	-99.0	2.760	H-long	Hβ, [O III]
XMM-LH	61	162.990	57.328	1.378	2+	1.379	1.188	H-short	Hα, [N II], [S II]
XMM-LH	63	163.151	57.267	1.729	2	1.734	1.649	J-long, H-long	Hβ, Hα, [N II]
XMM-LH	65	163.231	57.331	1.452	2	1.450	1.296	J-long, H-short, H-long	Hα, [N II], [S II]
XMM-LH	72	163.070	57.338	2.741	1	2.710	1.060	H-long	Hγ, [O III]
XMM-LH	85	163.373	57.351	1.144	2	1.145	0.469	J-long, H-short, H-long	Hα, [N II], [S II]
XMM-LH	96	163.187	57.356	2.826	1	2.832	-99.0	J-long, H-short, H-long	Hγ
XMM-LH	103	163.324	57.364	1.484	2++	-99.0	1.494	H-short, H-long	Hα, [N II]
XMM-LH	119	163.510	57.376	1.406	2++	-99.0	2.030	H-short, H-long	Hα, [N II], [S II]
XMM-LH	120	163.105	57.385	1.523	2	1.524	1.488	J-long, H-long	[O III], Hα, [N II], [S II]
XMM-LH	121	163.243	57.381	0.763	2	0.762	0.520	J-long, H-short, H-long	Hα, [N II], [S II]
XMM-LH	124	163.299	57.385	1.534	2	1.552	-99.0	H-long	Hα
XMM-LH	131	163.173	57.389	1.005	1	1.013	1.107	J-long, H-long	Hα
XMM-LH	136	163.050	57.389	0.743	1++	-99.0	1.170	H-short, H-long	[S III]
XMM-LH	151	163.483	57.399	1.398	2++	-99.0	1.445	H-short, H-long	Hα, [N II]
XMM-LH	154	163.609	57.401	0.963	2+	0.963	1.049	J-long	Hα
XMM-LH	156	162.977	57.402	2.391	2	2.367	0.544	J-long, H-short, H-long	Hβ
XMM-LH	167	163.574	57.406	1.220	1++	-99.0	1.406	H-short	Hα
XMM-LH	168	163.383	57.415	1.958	2	1.956	1.921	J-long, H-short, H-long	Hβ, [O III]
XMM-LH	171	163.588	57.429	0.205	2	0.205	0.214	J-long	[S III], He I
XMM-LH	174	162.837	57.416	1.186	1++	-99.0	1.168	H-short	Hα
XMM-LH	176	163.239	57.419	1.533	2	1.527	0.501	J-long, H-long	Hβ, Hα, [N II]
XMM-LH	179	163.132	57.417	1.475	1++	-99.0	1.480	H-short, H-long	Hα, [N II]
XMM-LH	183	163.301	57.418	1.877	2	1.876	1.603	J-long, H-short, H-long	[O III]
XMM-LH	191	163.396	57.428	0.787	2++	-99.0	0.967	J-long, H-short, H-long	Hα, [N II], [S II]
XMM-LH	203	163.500	57.434	1.742	2++	-99.0	1.772	H-long	Hα, [O I]
XMM-LH	217	162.799	57.443	0.760	1	0.758	0.734	J-long, H-long	Hα
XMM-LH	229	162.935	57.447	1.285	2++	-99.0	1.289	H-short, H-long	Hα, [N II]
XMM-LH	247	163.358	57.461	1.367	1++	-99.0	1.379	H-short	Hα
XMM-LH	254	163.181	57.466	1.183	1	1.210	0.968	J-long, H-short, H-long	Hα
XMM-LH	261	162.937	57.469	3.406	2	3.408	3.022	J-long, H-long	Mg II, [O II]
XMM-LH	267	163.352	57.472	1.549	2	1.563	1.420	J-long, H-long	[O III], Hα, [N II]
XMM-LH	268	163.450	57.471	1.295	1++	-99.0	1.298	H-short	Hα
XMM-LH	270	163.289	57.472	1.576	2	1.575	1.049	J-long, H-long	Hβ, Hα, [S II]
XMM-LH	277	163.437	57.478	1.807	1	1.816	1.945	J-long, H-long	Hγ
XMM-LH	279	163.192	57.472	1.514	1++	-99.0	1.460	H-short, H-long	Hα, [N II]
XMM-LH	300	163.266	57.490	0.789	2	0.788	0.504	J-long, H-short, H-long	Hα, [N II], [S II], [S III]
XMM-LH	306	163.028	57.490	0.709	1	0.709	0.677	J-long, H-long	[S III]
XMM-LH	321	163.102	57.502	1.008	2	1.009	1.543	J-long, H0long	Hα, [N II]
XMM-LH	340	163.130	57.504	1.212	2	1.212	1.034	H-short	Hα, [N II], [S II]
XMM-LH	342	163.416	57.518	0.587	2	0.586	0.533	J-long, H-short, H-long	[S III], He I
XMM-LH	354	162.856	57.514	3.409	2	3.409	2.945	J-long, H-short, H-long	Mg II, [O II]
XMM-LH	355	163.155	57.518	0.740	1	0.710	0.583	J-long, H-long	Hα, [S III]
XMM-LH	359	162.980	57.512	1.102	1++	-99.0	1.087	H-short	[S II]
XMM-LH	370	163.442	57.518	1.650	1++	-99.0	1.640	H-short, H-long	Hα, [N II]
XMM-LH	385	163.176	57.533	1.379	2	1.379	1.288	H-short	Hα, [N II]

TABLE2 – continued.

Field	ID	RA	Dec	Redshift	Quality	z_{spec}	z_{phot}	Band	Emission features
XMM-LH	386	163.058	57.528	0.894	2	0.896	0.849	J-long	Hα, [S II]
XMM-LH	387	163.249	57.532	1.449	2	1.447	1.398	H-short, H-long	Hα
XMM-LH	406	163.488	57.545	1.283	2	1.296	1.721	J-long, H-short	Hα
XMM-LH	409	163.403	57.550	1.600	2	1.601	0.504	J-long, H-long	Hα, [N II]
XMM-LH	419	163.501	57.556	1.491	1++	-99.0	1.491	H-long	Hα
XMM-LH	429	163.559	57.558	2.913	1++	-99.0	2.789	H-short, H-long	[O II]
XMM-LH	430	162.785	57.562	1.553	2	1.539	1.665	H-short, H-long	Hα
XMM-LH	443	163.155	57.567	1.877	2	1.877	1.823	J-long, H-short	[O III]
XMM-LH	450	163.275	57.573	2.952	2	2.945	2.529	J-long, H-short, H-long	[O II], Hγ, [O III]
XMM-LH	453	163.302	57.573	1.214	2	1.213	1.748	H-short	Hα, [S II]
XMM-LH	456	162.977	57.577	0.877	2	0.877	0.648	J-long, H-short, H-long	Hα, [N II], [S II], [S III]
XMM-LH	468	163.171	57.580	1.370	2++	-99.0	1.374	H-short	Hα, [S II]
XMM-LH	472	163.417	57.588	1.136	1	1.135	0.899	H-short	[S II]
XMM-LH	475	163.320	57.597	1.205	2++	-99.0	1.219	J-long, H-short, H-long	Hα, [N II]
XMM-LH	477	163.283	57.589	1.468	2++	-99.0	0.777	H-long	Hα
XMM-LH	488	163.369	57.594	0.690	1	0.700	0.584	H-long	[S III]
XMM-LH	518	163.401	57.624	2.269	2++	-99.0	2.563	H-short, H-long	[O III]
XMM-LH	521	163.176	57.621	1.591	1++	-99.0	1.526	H-long	Hα
XMM-LH	523	162.875	57.627	1.217	2++	-99.0	1.192	H-short, H-long	Hα, [N II]
XMM-LH	527	163.260	57.632	1.885	1	1.881	1.748	J-long, H-short	Hβ, [O III]
XMM-LH	528	163.151	57.628	2.341	1	2.352	2.076	H-short	Hγ, [O III]
XMM-LH	529	162.905	57.632	1.940	2+	1.910	1.997	J-long, H-short, H-long	[O III]
XMM-LH	530	162.844	57.626	1.474	2++	-99.0	1.426	H-short, H-long	Hα, [S II]
XMM-LH	532	163.190	57.629	1.675	2	1.677	0.534	J-long, H-long	Hβ, [O III], Hα, [N II], [S II]
XMM-LH	553	163.125	57.654	1.440	2	1.437	0.454	J-long, H-short, H-long	Hβ, [O III], Hα, [N II], [S II]
XMM-LH	555	162.967	57.652	1.674	2++	-99.0	2.080	H-short, H-long	Hα, [N II]
XMM-LH	560	163.216	57.652	1.724	1++	-99.0	1.650	H-long	Hα, [N II]
XMM-LH	563	163.379	57.656	1.379	2++	-99.0	1.559	H-short, H-long	Hα, [N II], [S II]
XMM-LH	569	163.240	57.663	0.947	1++	-99.0	1.044	H-short, H-long	[S III]
XMM-LH	572	163.343	57.669	0.750	1++	-99.0	0.730	H-short, H-long	[S III]
XMM-LH	588	163.068	57.686	1.409	2++	-99.0	1.272	H-short, H-long	Hα
XMM-LH	591	163.097	57.689	1.535	2	1.534	1.527	J-long, H-short, H-long	[O III], Hα, [N II], [S II]
XMM-LH	594	163.202	57.691	0.814	2+	0.814	1.087	J-long, H-long	Hα, [N II]
XMM-LH	595	162.932	57.689	1.602	2++	-99.0	1.583	H-long	Hα
XMM-LH	599	163.280	57.251	2.416	2	2.416	2.159	J-long, H-short, H-long	[O II], Hβ, [O III]
XMM-LH	604	163.299	57.704	2.104	2	2.113	1.932	J-long, H-short, H-long	Hβ, [O III]
XMM-LH	610	163.166	57.719	0.679	1+	0.679	0.675	J-long, H-short, H-long	[S II]
XMM-LH	999	163.105	57.380	0.809	2	0.807	0.659	J-long, H-short, H-long	Hα, [N II], [S II]
XMM-LH	1379	163.559	57.462	1.689	1++	-99.0	1.440	H-long	Hα
XMM-LH	1395	162.838	57.327	1.649	2++	-99.0	1.672	H-short, H-long	Hα
XMM-LH	1443	163.141	57.279	1.391	2++	-99.0	1.415	H-short	Hα
XMM-LH	1458	162.855	57.484	0.484	1	0.484	0.502	H-short	He I
XMM-LH	1476	163.360	57.651	1.235	1++	-99.0	1.300	H-short	Hα, [N II]
XMM-LH	1518	163.525	57.404	0.775	2++	-99.0	0.824	J-long, H-long	Hα
XMM-LH	1551	163.461	57.459	1.673	2++	-99.0	1.704	H-short, H-long	Hα, [N II]
XMM-LH	1595	163.071	57.610	1.545	1++	-99.0	1.580	H-long	Hα
XMM-LH	2015	163.258	57.508	1.357	1++	-99.0	1.370	H-short	Hα, [N II], [S II]
XMM-LH	2020	163.459	57.452	1.728	2+	1.720	1.442	J-long, H-long	Hα
XMM-LH	2081	163.035	57.346	1.356	1++	-99.0	1.296	H-short	Hα, [N II], [S II]
XMM-LH	2084	163.236	57.400	1.524	2++	-99.0	1.348	H-short, H-long	Hα, [N II], [S II]
XMM-LH	2254	163.123	57.726	2.945	2++	-99.0	2.803	H-short, H-long	Hγ
XMM-LH	2278	163.016	57.452	2.438	2	2.454	2.083	J-long, H-short, H-long	Hβ, [O III]
XMM-LH	2374	163.460	57.500	2.508	2++	-99.0	-99.0	H-long	[O III]
XMM-LH	2379	163.181	57.418	0.752	1++	-99.0	0.750	H-long	[S III]
XMM-LH	2380	163.423	57.507	2.063	1++	-99.0	2.095	H-short, H-long	Hβ, [O III]
XMM-LH	2506	162.890	57.590	2.010	2++	-99.0	2.016	J-long, H-short	[O III]

TABLE 3 Emission line properties of Broad-line AGNs

Field	ID	z	log L_{bol}	log M_{BH}	log FWHM (km s^{-1})			log L (erg s^{-1})		
			(erg s^{-1})	($M_\odot$)	Hα	Hβ	MgII	Hα	Hβ	3000Å
CDF-S	1	1.630	45.89±0.07	8.41±0.08	3.74±0.02	···	···	43.08±0.06	···	···
CDF-S	4	1.270	45.39±0.14	7.22±0.24	3.40±0.05	···	···	42.16±0.12	···	···
CDF-S	11	1.888	46.02±0.06	8.37±0.16	···	···	3.61±0.02	···	···	45.52±0.00
CDF-S	14	1.370	44.32±0.05	8.29±0.05	···	···	3.68±0.13	···	···	45.19±0.01
CDF-S	15	1.065	44.25±0.04	6.52±0.07	···	···	3.36±0.33	···	···	43.34±0.03
CDF-S	25	1.336	44.34±0.13	6.69±0.09	···	···	3.32±0.04	···	···	43.51±0.02
CDF-S	66	0.575	42.80±0.06	7.67±0.58	···	3.39±0.60	···	···	41.65±0.00	···
CDF-S	76	1.042	45.06±0.02	7.45±0.07	3.63±0.08	···	3.68±0.02	42.04±0.17		43.81±0.00
CDF-S	87	1.437	44.15±0.06	8.67±0.06	···	···	4.41±0.17	···	···	43.43±0.02
CDF-S	88	1.613	45.14±0.02	7.05±0.02	···	···	3.67±0.01	···	···	43.22±0.01
CDF-S	101	0.966	45.36±0.05	7.40±0.16	3.70±0.05	···	3.73±0.02	42.23±0.11	···	43.57±0.00
CDF-S	166	1.608	45.67±0.01	8.30±0.19	3.64±0.07	···	3.84±0.16	42.64±0.19	···	44.68±0.00
CDF-S	229	1.326	45.68±0.01	7.75±0.02	3.35±0.33	3.37±0.05	3.71±0.14	43.30±0.00	41.93±0.14	45.26±0.01
CDF-S	241	0.566	44.07±0.02	7.26±0.06	···	···	3.67±0.14	···	···	43.55±0.01

TABLE3 – continued.

Field	ID	z	log L_{bol} (erg s^{-1})	log M_{BH} ($M_\odot$)	log FWHM (km s^{-1}) Hα	Hβ	MgII	log L (erg s^{-1}) Hα	Hβ	3000Å
CDF-S	329	0.954	44.26±0.13	7.03±0.86	3.39±0.09	···	···	41.86±0.27	···	···
CDF-S	344	1.615	45.03±0.02	8.06±0.09	3.35±0.23	···	3.89±0.01	43.02±0.16	···	44.13±0.02
CDF-S	367	1.041	45.45±0.00	7.27±0.38	···	···	3.39±0.02	···	···	44.46±0.00
CDF-S	369	1.612	45.53±0.02	7.46±0.82	3.47±0.16	···	···	42.35±0.15	···	···
CDF-S	375	0.742	45.76±0.00	8.14±0.02	3.78±0.24	···	3.81±0.01	43.12±0.03	···	44.51±0.01
CDF-S	417	1.222	45.33±0.01	8.91±0.14	4.03±0.15	···	···	42.90±0.12	···	···
CDF-S	420	0.960	44.09±0.03	7.35±0.30	3.38±0.65	···	···	42.47±0.00	···	···
CDF-S	473	1.557	45.82±0.02	7.84±0.52	3.50±0.59	···	···	42.92±0.00	···	···
CDF-S	514	0.664	44.03±0.03	7.46±0.61	···		3.85±0.27	···	···	43.27±0.00
CDF-S	523	0.838	45.43±0.01	8.35±0.03	3.69±0.40	···	4.11±0.29	43.14±0.00	···	44.56±0.03
CDF-S	537	1.216	44.87±0.02	8.60±0.16	···	···	3.96±0.17	···	···	44.76±0.02
CDF-S	614	0.664	43.18±0.06	8.23±0.03	···	···	4.14±0.02	···	···	43.58±0.02
CDF-S	627	0.736	44.80±0.01	7.29±0.12	···	···	3.72±0.02	···	···	43.43±0.02
CDF-S	656	1.367	43.66±0.07	7.45±0.49	3.36±0.49	···	···	42.72±0.00	···	···
CDF-S	681	0.733	44.34±0.02	7.28±0.11	···	···	3.65±0.11	···	···	43.65±0.00
CDF-S	691	2.005	45.93±0.05	8.95±0.39	···	···	3.81±0.15	···	···	45.82±0.01
CDF-S	695	0.622	43.79±0.03	7.65±0.05	···	···	3.87±0.04	···	···	43.51±0.02
CDF-S	720	1.609	45.94±0.02	8.50±0.12	3.85±0.04	···	···	42.81±0.08	···	···
CDF-S	723	2.072	45.66±0.05	8.82±0.02	···	···	3.82±0.01	···	···	45.55±0.02
CDF-S	724	1.337	44.95±0.07	7.69±0.16	3.52±0.30	···	···	42.81±0.00	···	···
E-CDF-S	7	1.368	46.16±0.00	9.30±0.04	4.12±0.02	···	3.90±0.00	43.27±0.04	···	45.29±0.02
E-CDF-S	53	1.524	45.58±0.00	9.18±0.19	···	···	4.03±0.18	···	···	45.48±0.02
E-CDF-S	68	1.362	44.58±0.03	8.55±0.06	···	···	3.77±0.03	···	···	45.30±0.02
E-CDF-S	89	1.613	44.44±0.16	7.32±0.14	3.44±0.08	···	···	42.22±0.17	···	···
E-CDF-S	100	1.957	45.64±0.01	8.69±0.12	···	···	3.73±0.13	···	···	45.65±0.01
E-CDF-S	158	0.717	44.44±0.01	8.81±0.08	···	3.89±0.02	···	···	41.88±0.03	···
E-CDF-S	166	1.408	44.81±0.02	8.31±0.61	3.70±0.42	···	···	43.02±0.00	···	···
E-CDF-S	193	1.167	44.54±0.01	8.45±0.04	···	···	3.83±0.02	···	···	44.96±0.05
E-CDF-S	358	1.626	45.64±0.00	8.29±0.02	3.42±0.43	3.73±0.09	3.61±0.00	43.59±0.00	41.95±0.21	45.38±0.01
E-CDF-S	381	0.526	44.28±0.00	7.72±0.34	···	3.63±0.17	···	···	40.87±0.19	···
E-CDF-S	517	1.345	44.94±0.00	7.82±0.30	3.64±0.08	···	···	42.37±0.23	···	···
E-CDF-S	601	1.598	45.47±0.02	7.55±0.35	3.41±0.59	···	···	42.74±0.00	···	···
E-CDF-S	631	2.072	45.49±0.01	8.67±0.24	···	···	3.79±0.06	···	···	45.42±0.05
E-CDF-S	678	1.629	45.30±0.00	8.58±0.06	3.77±0.18	···	3.73±0.21	43.25±0.07	···	45.43±0.01
E-CDF-S	681	0.834	44.66±0.00	8.41±0.06	3.88±0.02	···	···	42.53±0.04	···	···
E-CDF-S	700	2.171	45.78±0.00	8.31±0.24	···	···	3.91±0.19	···	···	44.45±0.02
E-CDF-S	712	0.841	45.74±0.00	8.00±0.02	3.76±0.34	···	3.73±0.01	42.66±0.00	···	44.55±0.07
E-CDF-S	716	0.763	44.93±0.00	8.11±0.43	3.70±0.33	···	···	42.65±0.00	···	···
E-CDF-S	725	1.314	45.74±0.00	8.31±0.10	3.59±0.23	···	3.71±0.01	43.11±0.13	···	45.12±0.02
E-CDF-S	728	1.583	45.44±0.01	8.54±0.19	3.81±0.03	···	···	43.02±0.05	···	···
E-CDF-S	742	1.762	44.85±0.03	8.33±0.18	···	···	3.60±0.03	···	···	45.48±0.01
XMM-LH	5	2.138	46.55±0.01	8.24±0.08	···	3.35±0.54	···	···	42.77±0.00	···
XMM-LH	25	1.599	44.52±0.32	7.52±0.65	3.50±0.07	···	···	42.36±0.17	···	···
XMM-LH	41	1.653	45.89±0.08	8.09±0.20	···	···	3.71±0.15	···	···	44.75±0.02
XMM-LH	85	1.144	45.26±0.01	8.03±0.02	···	···	3.75±0.18	···	···	44.52±0.02
XMM-LH	119	1.406	45.25±0.07	8.55±0.08	3.83±0.02	···	···	42.97±0.03	···	···
XMM-LH	120	1.523	45.65±0.02	7.62±0.16	3.54±0.09	···	···	42.39±0.25	···	···
XMM-LH	148	1.116	46.58±0.00	8.93±0.06	···	···	3.74±0.13	···	···	46.02±0.01
XMM-LH	168	1.958	46.95±0.01	8.85±0.23	···	3.74±0.06	···	···	42.49±0.14	···
XMM-LH	176	1.533	45.77±0.01	8.12±0.04	3.43±0.01	···	3.55±0.01	43.19±0.02	···	45.30±0.01
XMM-LH	191	0.787	45.94±0.01	7.94±0.02	3.86±0.01	···	3.82±0.18	42.53±0.02	···	44.16±0.02
XMM-LH	261	3.406	46.77±0.05	7.58±0.05	···	···	3.37±0.00	···	···	45.02±0.02
XMM-LH	270	1.576	45.66±0.01	8.39±0.06	3.75±0.01	3.55±0.05	3.73±0.14	43.50±0.02	41.93±0.11	45.17±0.01
XMM-LH	321	1.008	45.04±0.03	7.44±0.03	···	···	3.55±0.01	···	···	44.24±0.00
XMM-LH	332	1.676	46.31±0.01	8.08±0.02	···	···	3.74±0.02	···	···	44.64±0.01
XMM-LH	354	3.409	46.95±0.02	8.93±0.17	···	···	3.76±0.16	···	···	45.93±0.02
XMM-LH	364	0.932	44.53±0.03	7.55±0.09	···	···	3.65±0.04	···	···	44.09±0.02
XMM-LH	387	1.449	45.04±0.02	7.58±0.06	3.38±0.02	···	3.47±0.01	42.90±0.03	···	44.61±0.02
XMM-LH	406	1.283	45.39±0.06	8.77±0.02	3.92±0.01	···	3.80±0.03	43.03±0.01	···	44.86±0.01
XMM-LH	430	1.553	46.48±0.02	8.33±0.17	···	···	3.90±0.17	···	···	44.54±0.02
XMM-LH	453	1.214	45.02±0.06	7.41±0.04	···	···	3.52±0.02	···	···	44.26±0.02
XMM-LH	456	0.877	45.28±0.02	7.44±0.30	3.62±0.06	···	···	41.76±0.15	···	···
XMM-LH	475	1.205	47.07±0.01	8.90±0.00	3.69±0.00	···	3.87±0.14	44.13±0.00	···	45.66±0.01
XMM-LH	523	1.217	45.65±0.06	7.84±0.08	3.60±0.03	···	···	42.57±0.08	···	···
XMM-LH	529	1.940	46.74±0.04	8.55±0.11	···	3.68±0.09	···	···	42.16±0.20	···
XMM-LH	532	1.675	45.01±0.03	8.29±0.31	3.60±0.03	···	3.73±0.02	42.91±0.06	···	45.01±0.01
XMM-LH	553	1.440	46.36±0.01	8.68±0.03	3.76±0.01	···	···	43.49±0.02	···	···
XMM-LH	555	1.674	45.84±0.03	8.99±0.13	4.01±0.04	···	···	43.11±0.07	···	···
XMM-LH	591	1.535	45.65±0.05	8.22±0.08	3.62±0.32	···	···	43.18±0.00	···	···
XMM-LH	595	1.602	45.08±0.09	8.50±0.29	3.78±0.27	···	···	43.09±0.07	···	···
XMM-LH	604	2.104	46.47±0.02	8.66±0.83	···	3.54±0.62	···	···	42.86±0.00	···
XMM-LH	2020	1.728	45.96±0.01	7.98±0.10	3.55±0.01	···	···	42.99±0.02	···	···

REFERENCES

Allevato, V., Finoguenov, A., Cappelluti, N., et al. 2011, ApJ, 736, 99

Babić, A., Miller, L., Jarvis, M. J., et al. 2007, A&A, 474, 755

Barger, A. J., Cowie, L. L., Mushotzky, R. F., et al. 2005, AJ, 129, 578
Barger, A. J., et al. 2014, priv. comm.
Bongiorno, A., Zamorani, G., Gavignaud, I., et al. 2007, A&A, 472, 443
Brandt, W. N. & Hasinger, G. 2005, ARA&A, 43, 827
Brandt, W. N. & Alexander, D. M. 2010, PNAS, 107, 7184
Brunner, H., Cappelluti, N., Hasinger, G., et al. 2008, A&A, 479, 283
Choi, E., Ostriker, J. P., Nabb, T., et al. 2012, ApJ, 754, 125
Choi, Y., Gibson, R. R., Becker, A., et al. 2014, ApJ, 782, 37
Cirasuolo, M., McLure, R. J., Dunlop, J. S., et al. 2007, MNRAS, 380, 585
Cisternas, M., Jahnke, K., Inskip, K. J., et al. 2011, ApJ, 726, 57
Cowie, L. L., Barger, A. J., Bautz, M. W., et al. 2003, ApJ, 584L, 57
Di Matteo, T., Springel, V., Hernquist, L. 2005, Nature, 433, 604
Fabian, A. C. 1999, MNRAS, 308, 39
Fabian, A. C., Vasudevan, R. V., Gandhi, P. 2008, MNRAS, 385, 43
Fan, L., Fang, G., Chen, Y., et al. 2014, ApJ Letters, 784, L9
Fanidakis, N., Baugh, C. M., Benson, A. J., et al. 2012, MNRAS, 419, 2797
Ferrarese, L. & Merritt, D. 2000, ApJ, 539, 9
Fotopoulou, S., Salvato, M., Hasinger, G., et al. 2012, ApJS, 198, 1
Gabor, J. M., Impey, C. D., Jahnke, K., et al. 2009, ApJ, 691, 705
Gavignaud, I., Wisotzki, L., Bongiorno, A., et al. 2008, A&A, 492, 637
Gebhardt, K., Bender, R., Bower, G., et al. 2000, ApJ, 539, 13
Giacconi, R., Zirm, A., Wang, J., et al. 2002, ApJS, 139, 369
Graham, A. W., Onken, C. A., Athanassoula, E., et al. 2011, MNRAS, 412, 2211
Greene, J. E., & Ho, L. C. 2005, ApJ, 630, 122
Gültekin, K., Richstone, D., Gebhardt, K., et al. 2009, ApJ, 698, 198
Harris, K. A., Williger, G. M., Haberzettl, L., et al. 2013, MNRAS, 435, 3125
Hasinger, G., ltieri, B., Arnaud, M., et al. 2001, A&A, 365L, 45
Hasinger, G., Miyaji, T., Schmidt, M. 2005, A&A, 441, 417
Hasinger, G. 2008, A&A, 490, 905
Hopkins, P. F., & Hernquist, L. 2006, ApJS, 166, 1
Hopkins, P. F., Richards, G. T., Hernquist, L. 2007, ApJ, 654, 731
Iwamuro, F., Moritani, Y., Yabe, K., et al. 2012, PASJ, 64, 59
Ji, I., Peirani, S., Yi, S. K. 2014, arXiv:1405.1807v1
Kaspi, S., Smith, P. S., Netzer, H., et al. 2000, ApJ, 533, 631
Kelly, B. C., Vestergaard, M., Fan, X., et al. 2010, ApJ, 719, 1315
Kimura, M., et al. 2010, PASJ, 62, 1135
Kocevski, D. D., Faber, S. M., Mozena, M. et al. 2012, ApJ, 744, 148
Kollmeier, J. A., Onken, C. A., Kochanek, C. S., et al. 2006, ApJ, 648, 128
Kormendy, J., & Richstone, D. 1995, ARA&A, 33, 581
La Franca, F., Fiore, F., Comastri, A., et al. 2005, ApJ, 635, 864
Lehmann, I., Hasinger, G., Schmidt, M., et al. 2000, A&A, 354, 34
Lehmann, I., Hasinger, G., Schmidt, M., et al. 2001, A&A, 371, 833
Lehmer, B. D., Brandt, W. N., Alexander, D. M., et al. 2005, ApJS, 161, 21
Lockman, F. J., Jahoda, K., & McCammon, D. 1986, ApJ, 302, 432
Lotz, J. M., Jonsson, P., Cox, T. J., & Primack, J. R. 2008, MNRAS, 391, 1137
Lusso, E., Comastri, A., Vignali, C., et al., 2010, A&A, 512, 34
Lusso, E., Comastri, B. D., Simmons, M. M., et al. 2012, MNRAS, 425, 623
Madau, P. & Dickinson, M. 2014, arXiv:1403.0007v2
Magorrian, J., Tremaine, S., Richstone, D., et al. 1998, AJ, 115, 2285
Mainieri, V., Bongiorno, A., Merloni, A. 2011, A&A, 535, A80
Marconi, A., Risaliti, G., Gilli, R., et al. 2004, MNRAS, 351, 169
Masters, D., & Capak, P. 2011, PASP, 123, 638
Matsuoka, Y., Oyabu, S., Tsuzuki, Y., Kawara, K. 2007, ApJ, 663, 781
Matsuoka, K., Silverman, J. D., Schramm, M., et al. 2013, ApJ, 771, 64
McConnell, N. J., & Ma, C.-P. 2013, ApJ, 764, 184
McGill, K. L., Woo, J., Treu, T., Malkan, M. A. 2008, ApJ, 673, 703
McLure, R. J., & Dunlop, J. S. 2004, MNRAS, 352, 1390
McLure, R. J, & Jarvis, M. J. 2002, MNRAS, 337, 109
Merloni, A., & Heinz, S. 2008, MNRAS, 388, 1011
Merloni, A., Bongiorno, A., Bolzonella, M., et al. 2010, ApJ, 708, 137
Merritt, D., & Ferrarese, L. 2001, ApJ, 547, 140
Mullaney, J. R., Pannella, M., Daddi, E., et al. 2012, MNRAS, 419, 95
Nobuta, K., Akiyama, M., Ueda, Y. et al. 2012, ApJ, 761, 143
Rafiee, A., & Hall, P. B. 2011, ApJS, 194, 42
Rosario, D. J., McIntosh, D. H., van der Wel, A., et al. 2015, A&A, 573, 85
Rovilos, E., Fotopoulou, S., Salvato, M., et al. 2011, A&A, 529, 135
Schawinski, K., Urry, C. M., Virani, S., et al. 2010, ApJ, 711, 284
Schawinski, K., Treister, E., Urry, C. M. et al. 2011, ApJ Letters, 727, L31
Schawinski, K., Simmons, B. D., Urry, C. M., et al. 2012, MNRAS, 425, L61
Schneider, D. P., Richards, G. T., Hall, P. B., et al. 2010, AJ, 139, 2360
Scharamm, M., and Silverman, J. D. 2013, ApJ, 767, 13
Schulze, A., & Gebhardt, K. 2011, ApJ, 729, 21
Schulze, A., & Wisotzki, L. 2010, A&A, 516, 87
Shankar, F., Weinberg D, Miralda-Escude, J. 2009, ApJ, 690, 20
Shen, Y., & Liu, X. 2012, ApJ, 753, 125
Shen, Y., Greene, J. E., Strauss, M. A., et al. 2008, ApJ, 680, 169
Shen, Y., Richards, G. T., Strauss, M. A., et al. 2011, ApJS, 194, 45
Silverman, J. D., Mainieri, V., Lehmer B. D., et al. 2008, ApJ, 675, 1025
Silverman, J. D., Green, P. J., Barkhouse, W. A., et al. 2008, ApJ, 679, 118
Silverman, J. D., Mainieri, V., Salvato, M., et al. 2010, ApJS, 191, 124
Silverman, J. D., Kampczyk, P., Jahnke, K., et al. 2011, ApJ, 743, 2
Simpson, C. 2005, MNRAS, 360, 565
Springel, V., Di Matteo, T., & Hernquist, L. 2005, MNRAS, 361, 776
Stark, A. A., Gammie, C. F., Wilson, R. W., et al. 1992, ApJS, 79, 77
Steffen, A. T., Barger, A. J., Cowie, L. L., et al. 2003, ApJ, 596L, 23
Steinhardt, C. L., & Elvis, M. 2010, MNRAS, 402, 2637
Szokoly, G. P., Bergeron, J., Hasinger, G., et al. 2004, ApJS, 155, 271
Tremaine, S., Gebhardt, K., Bender, R., et al. 2002, ApJ, 574, 740
Trump, J. R., Impey, C. D., Kelly, B. C., et al. 2011, ApJ, 733, 60
Ueda, Y., Akiyama, M., Ohta, K., et al. 2003, ApJ, 598, 886
Vasudevan, R. V., and Fabian, A. C. 2007, MNRAS, 381, 1235
Vestergaard, M. 2002, ApJ, 571, 733
Vestergaard, M., & Osmer, P. S. 2009, ApJ, 699, 800
Vestergaard, M., & Peterson, B. M. 2006, ApJ, 641, 689
Vestergaard, M., & Wilkes, B. J. 2001, ApJS, 134, 1
Vignali C., Brandt W. N., Schneider D. P., 2003, AJ, 125, 433
Villforth, C., Hamann, F., Rosario, D. J., et al. 2014, MNRAS, 439, 3342
Wang, J., Dong, X., Wang, T. et al. 2009, ApJ, 707, 1334
Woo, J., & Urry, C. M. 2002, ApJ, 579, 530
Woo, J., Schulze, A., Park, D. et al. 2013, ApJ, 772, 49
Xue, Y. Q., Luo, B., Brandt, W. N., et al. 2011, ApJS, 195, 10